Mesoscale to Submesoscale Transition in the California Current System. Part II: Frontal Processes

X. CAPET, J. C. MCWILLIAMS, M. J. MOLEMAKER, AND A. F. SHCHEPETKIN

Institute of Geophysics and Planetary Physics, University of California, Los Angeles, Los Angeles, California

(Manuscript received 2 August 2006, in final form 13 April 2007)

ABSTRACT

This is the second of three papers investigating the regime transition that occurs in numerical simulations for an idealized, equilibrium, subtropical, eastern boundary, upwelling current system similar to the California Current. The emergent upper-ocean submesoscale fronts are analyzed from phenomenological and dynamical perspectives, using a combination of composite averaging and separation of distinctive subregions of the flow. The initiating dynamical process for the transition is near-surface frontogenesis. The frontal behavior is similar to both observed meteorological surface fronts and solutions of the approximate dynamical model called surface dynamics (i.e., uniform interior potential vorticity q and diagnostic force balance) in the intensification of surface density gradients and secondary circulations in response to a mesoscale strain field. However, there are significant behavioral differences compared to the surface-dynamics model. Wind stress acts on fronts through nonlinear Ekman transport and creation and destruction of potential vorticity. The strain-induced frontogenesis is disrupted by vigorous submesoscale frontal instabilities that in turn lead to secondary frontogenesis events, submesoscale vortices, and excitation of even smaller-scale flows. Intermittent, submesoscale breakdown of geostrophic and gradient-wind force balance occurs during the intense frontogenesis and frontal-instability events.

1. Introduction

In Capet et al. (2008, hereinafter Part I), a suite of computational simulations for an idealized subtropical, eastern boundary, upwelling current system [referred to as the idealized California Current (ICC)] is analyzed for the emergent submesoscale flows that arise once the horizontal grid resolution increases to $O(1)$ km. The high-resolution solutions (ICC0 at 0.750-km and ICC1 at 1.5-km horizontal grid spacing) exhibit abundant near-surface submesoscale features, especially in between the mesoscale eddies. These features are conspicuous in tracer (Fig. 1), velocity, and vorticity fields with a high degree of correlation among them (Figs. 4 and 5 of Part I). In particular, the correlation between vertical velocity w and the thermohaline fields (i.e., potential temperature T, salinity S, and potential density ρ) at the submesoscale implies significant vertical thermohaline eddy fluxes, absent or much weaker at lower resolutions. This adds to a growing body of evidence, observational and numerical, that the submesoscale range is more than just passive fine structure for the quasigeostrophic mesoscale regime. In classical quasigeostrophy there is little energy on scales below the first baroclinic deformation radius R_1, and the tracer variance at these scales is controlled almost entirely by mesoscale eddy stirring (i.e., nonlocally in wavenumber).

The ubiquity of mesoscale eddies in the ocean is associated with a preferred length scale—the first baroclinic deformation radius R_1—where kinetic energy tends to accumulate. Quasigeostrophic theory (e.g., Pedlosky 1987) provides a framework for understanding this behavior as a combination of inverse energy cascade and/or forward potential enstrophy cascade on scales smaller than R_1; inhibition of inverse cascade by topography and Coriolis-frequency gradients to scales much larger than R_1; potential-to-kinetic energy conversion around R_1; and a large potential-to-kinetic energy partition ratio on larger scales. An analogous conceptual framework has yet to be established for the submesoscale regime. The aim of this paper is to describe the dominant dynamical processes associated

---

Corresponding author address: Xavier Capet, IGPP/UCLA, 405 Charles E. Young Dr., Los Angeles, CA 90095-1567.
E-mail: capet@atmos.ucla.edu

DOI: 10.1175/2007JPO3672.1

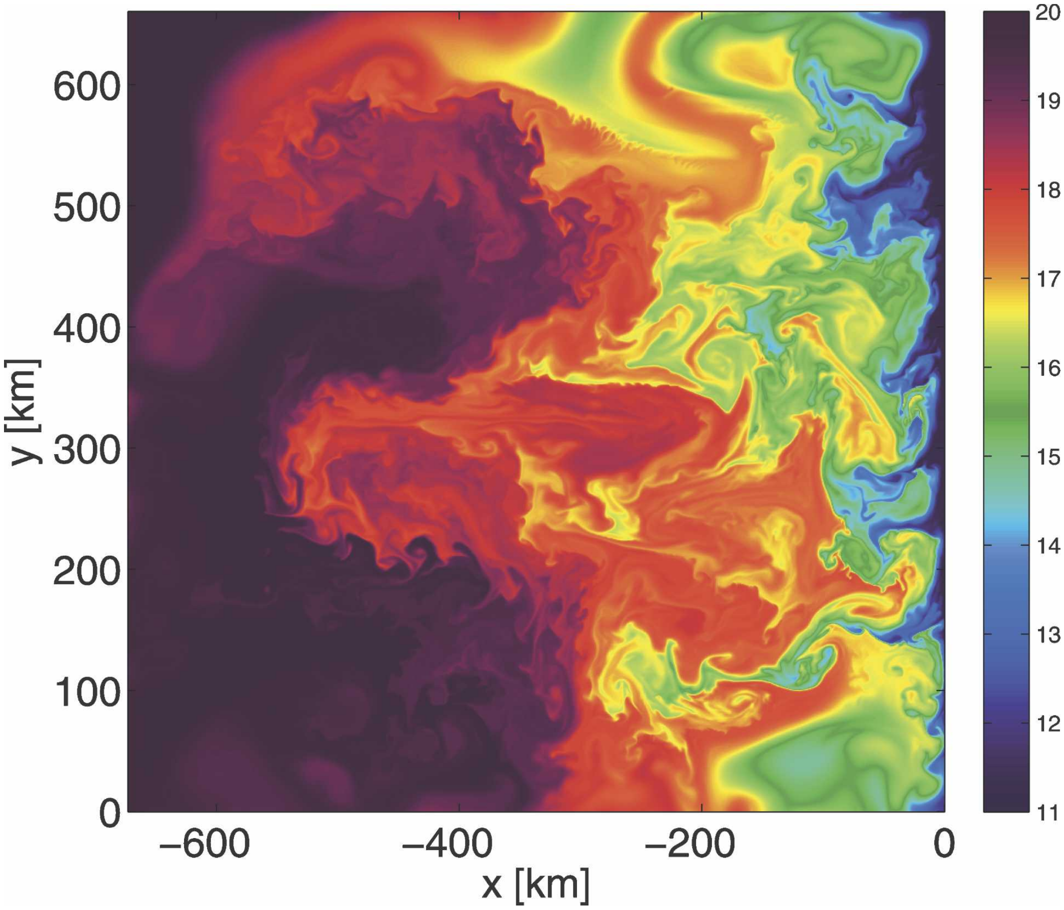

FIG. 1. Instantaneous surface temperature $T(x, y)$ field at time $t = 208$ days after ICC initialization. Note the string of meanders and filaments in 17°–19°C water with wavelengths ≈50 km running along the edges of the offshore eddies. The particular instability event labeled case 3 (section 4b) is located at ($x \approx -250$ km, $y \approx 350$ km); it separates waters in the range 16°–18°C, and the temperature front is roughly aligned with the x axis.

with submesoscale flow structures and to assess the degree that existing simpler models (interior quasigeostrophic, surface quasigeostrophic, and balanced dynamics) are apt. Submesoscale frontogenesis is examined in section 2. The direct effect of wind forcing on submesoscale fronts is the subject of section 3. The submesoscale instabilities present in our solutions and their dynamical roles are considered in section 4. The validity of the diagnostic force balance approximation is assessed in section 5. Section 6 is a synthesis of our present view of the submesoscale regime as middle path between two prevailing views on the submesoscale that emphasize either frontogenesis/eddy-stirring (Lapeyre et al. 2006) or surface-layer instability (Boccaletti et al. 2007). A summary is in section 7. The submesoscale kinetic energy balance is analyzed in the third paper of this sequence (Capet et al. 2006, manuscript submitted to *J. Phys. Oceanogr.*, hereinafter Part III).

2. Frontogenesis

a. Surface fronts and secondary circulation

A key element of the upper-ocean submesoscale transition—occurring strongly in ICC0 and to a lesser extent in ICC1 and ICC3—is frontogenesis (Fig. 2). The theory of frontogenesis for cross-front density gradient intensification (Stone 1966a; Hoskins and Bretherton 1972; Hoskins 1982) involves initiation by larger-scale (mesoscale here) straining, disruption of the geostrophic balance for the alongfront flow, and generation of an ageostrophic secondary circulation (i.e., in the cross-front plane). The secondary circulation acts to restore geostrophic balance by advectively tilting isopycnals toward the horizontal (i.e., restratification) and accelerating the geostrophic flow, hence resisting horizontal density gradient strengthening. To do this effectively, the secondary circulation develops vertical ve-

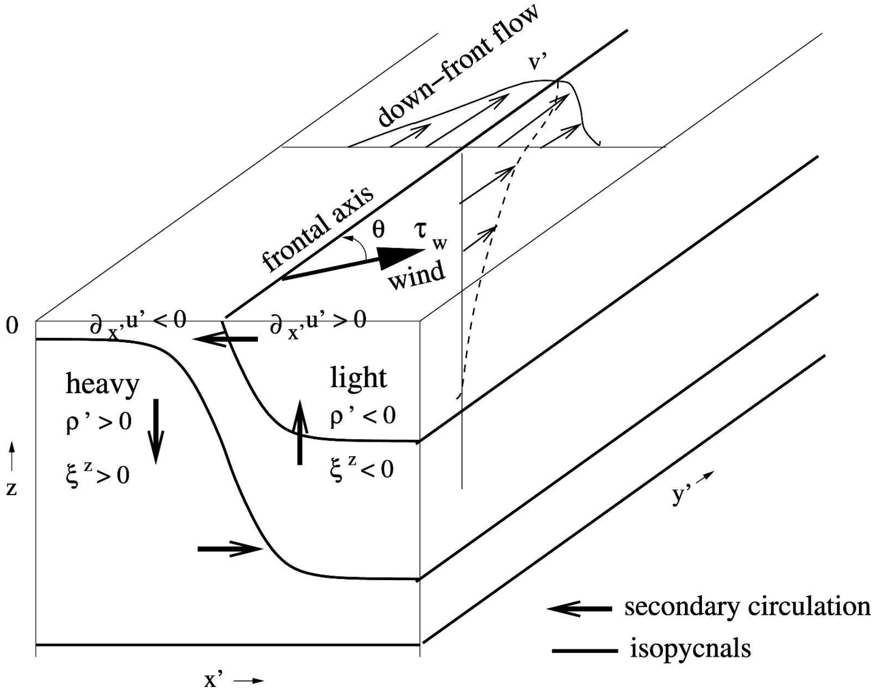

FIG. 2. Schematic configuration for an intensifying straight surface front with $f > 0$; (x_*, y_*) and (u_*, v_*) are rotated horizontal coordinates and velocity aligned with the frontal axis and its approximately geostrophic jet flow, and $\delta\rho$ is the local potential density perturbation. Also shown is the orientation angle θ relative to the surface wind stress.

locities (denoted w), upward on the light (warm) side and downward on the heavy (cold) side. However, near the surface where $w \approx 0$, $\partial_z w$ is large, and hence the surface ageostrophic horizontal divergence is large, frontogenesis can proceed even more rapidly, overcoming the restratification effect. Furthermore, through vertical vortex stretching,

$$\frac{D\zeta^z}{Dt} \approx (f + \zeta^z)\frac{\partial w}{\partial z}, \tag{1}$$

strong vertical vorticity ζ^z is generated, especially on the cyclonic (heavy) side of the alongfront flow (cf. Fig. 4 of Part I; Hakim et al. 2002). This characterization is for a straight front without surface stress, but it also has validity for curved fronts. The presence of a surface wind stress modifies this picture somewhat (section 3b).

To investigate frontogenesis we introduce

$$\frac{D|\nabla_h \rho|^2}{Dt} = F, \tag{2}$$

as commonly done (Hoskins 1982); ρ is potential density, and F can be decomposed into several contributing terms (section 2b). At the mesoscale we expect frontogenesis to be instigated by the horizontal advective contribution,

$$F_s = \mathbf{Q}_s \cdot \nabla_h \rho, \tag{3}$$

with

$$\mathbf{Q}_s = -(\partial_x u \partial_x \rho + \partial_x v \partial_y \rho,\ \partial_y u \partial_x \rho + \partial_y v \partial_y \rho), \tag{4}$$

where F_s is a measure of the rate of increase for the horizontal density gradient arising from the straining by the horizontal velocity field (Hoskins 1982); also see further analysis in section 2b. As in Part I, x and y are horizontal coordinates in the cross-shore and alongshore directions, and u and v are the corresponding horizontal velocity components.

Typical horizontal patterns of the frontally concentrated quantities $|\nabla_h \rho|$, w, $w''T''$, and F_s are shown in Fig. 3. (Herein $''$ refers to the spatial and temporal high-pass filtering introduced in section 6 of Part I to isolate submesoscale flow and tracer components.) All of these quantities are mutually related in a way that is suggestive of ongoing frontogenesis. Most important, the extrema of w, $w''T''$, and ζ^z are localized in regions where the velocity field is conducive to frontogenesis, that is, where F_s is large, as expected from frontogenesis theory (Hoskins and Bretherton 1972). However, there is no pointwise correspondence because of the spatial structure of secondary circulations around fronts, and the strength of the correspondence varies from one feature

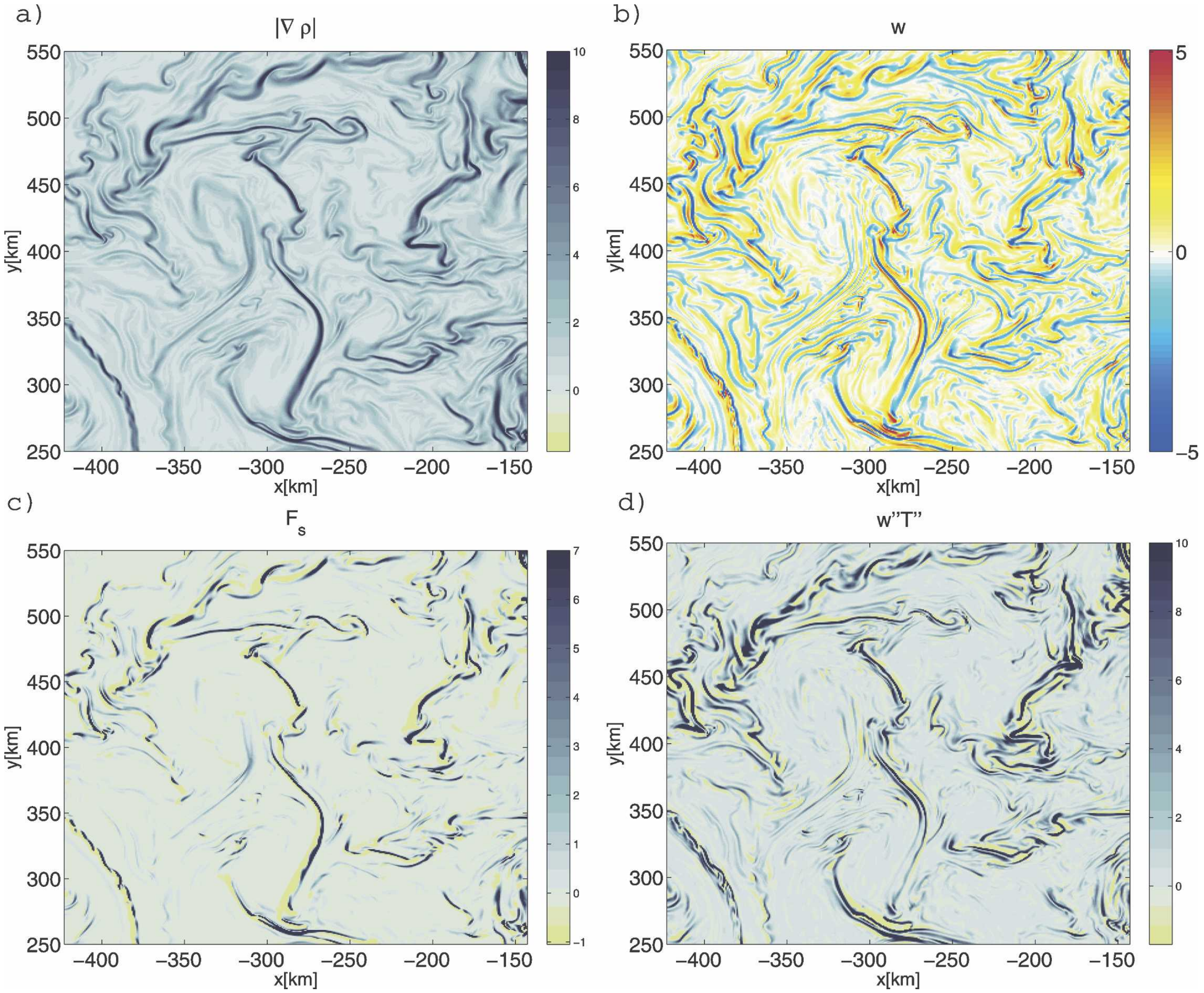

FIG. 3. Instantaneous horizontal patterns for frontal quantities in ICC0 at t = 160 days and 10-m depth in a 270 km × 300 km subdomain: (a) $|\nabla_h \rho|$ (10^{-5} kg m^{-4}), (b) $|w|$ (10^{-4} m s^{-1}), (c) F_s (10^{-14} kg^2 m^{-8} s^{-1}), and (d) $w''T''$ (10^{-5} m°C s^{-1}).

to another. Indeed, there is a structural difference between w and $\nabla_h \rho$ on one side and F_s and $w''T''$ on the other side. The latter pair of variables is more spatially intermittent, as seen in the horizontal section in Fig. 4. Intuitively, if intensifying fronts are thought of as linear delta functions for the density gradient, vorticity, and vertical velocity (ignoring for simplicity the fact that the latter two quantities actually change sign on each side of the front), $w''T''$ and F_s are products of such delta functions.[1] More fundamentally, the general relationships between these different quantities are complex and involve processes other than frontogenesis (e.g., Lapeyre et al. 2006, and section 4 herein).

To assess the significance of frontogenesis for the ICC0 simulation, we define the function $\delta_n(x, y) = 2\rho - \max_{\mathcal{S}_n}(\rho) - \min_{\mathcal{S}_n}(\rho)$, where $\mathcal{S}_n$ is the local (X, Y) domain, $[x - n\Delta x \le X \le x + n\Delta x, y - n\Delta x \le Y \le y + n\Delta x]$ for any integer n; δ_n is a finite-region approximation to a second derivative of ρ; and δ_n will be largest on the edges of frontal regions with $\delta_n < 0$ on the light side and $\delta_n > 0$ on the heavy. We present results for $n = 2$, matching the small horizontal scale achieved by fronts in our solution, although they are not qualitatively sensitive in the range n = 1 to 4. Figure 5 illustrates ρ, $|\nabla_h \rho|$, δ_2, and w for an adjacent pair of typical frontal structures in ICC0: one is straight over a mesoscale distance, and the other is fragmented and curved, suggestive of

---

[1] This is obvious for $w''T''$. Rewriting F_s for the straight front depicted in Fig. 2, we have $F_s = -\partial_{y_*} v_* (\partial_{y_*} \rho)^2$; that is, it is at least quadratic. Since v_* can also be frontally concentrated, F_s tends to be even more singular than $w''T''$, as Fig. 4 also suggests.

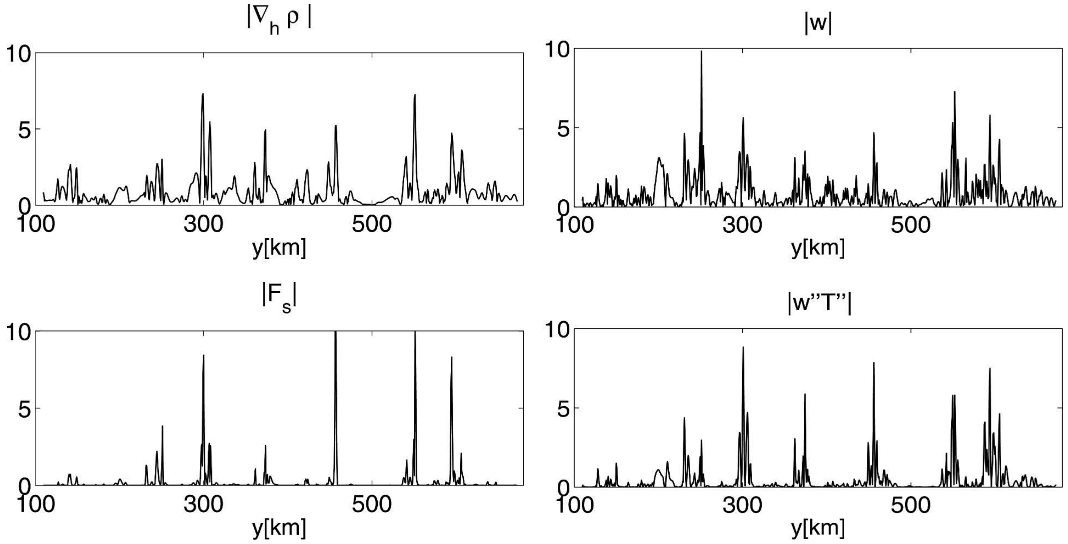

FIG. 4. A randomly chosen 570-km section for the frontal quantities in Fig. 3. For each quantity the absolute value is taken and normalized by the root-mean-square values along the section.

frontal breakup (section 4). Their structure is consistent with the frontogenetic theoretical expectation sketched in Fig. 2, and the frontal indexes adequately discriminate their target regions, as is generally the case.

Composite vertical profiles of w, $w''T''$, ζ^z, and F_s are shown in Fig. 6. The compositing is done over all frontal regions within the domain from 50 independent times in ICC0. The grid points retained in the averaging are those verifying $|\nabla_h \rho| > 1.2 \times 10^{-4}$ kg m^{-4} and $|\delta_2| > 0.1$ kg m^{-3} for the cold and warm sides. In doing so, we retain respectively 2.5% of the domain area for the frontal compositing and 0.6% for the cold/warm-side compositings. Notice that the 2.5% value seems roughly consistent with the probability of detecting SST fronts off California estimated by Castelao et al. (2006). The signatures of strong frontogenesis are evident in the profiles of Fig. 6. Upward velocities (light side) are much weaker than downward velocities (heavy side) and nearly zero in the center, as predicted by theory (Hoskins 1982). The extrema of w ($\approx$20 m day^{-1} on the light side, and -50 m day^{-1} on the heavy side) are found 10–15 m below the surface, that is, at the depth where the vertical heat flux divergence changes sign (see Fig. 11 of Part I). Cyclonic vorticities (heavy side) are much stronger than anticyclonic vorticities (light side), as expected from the asymmetry of vortex-

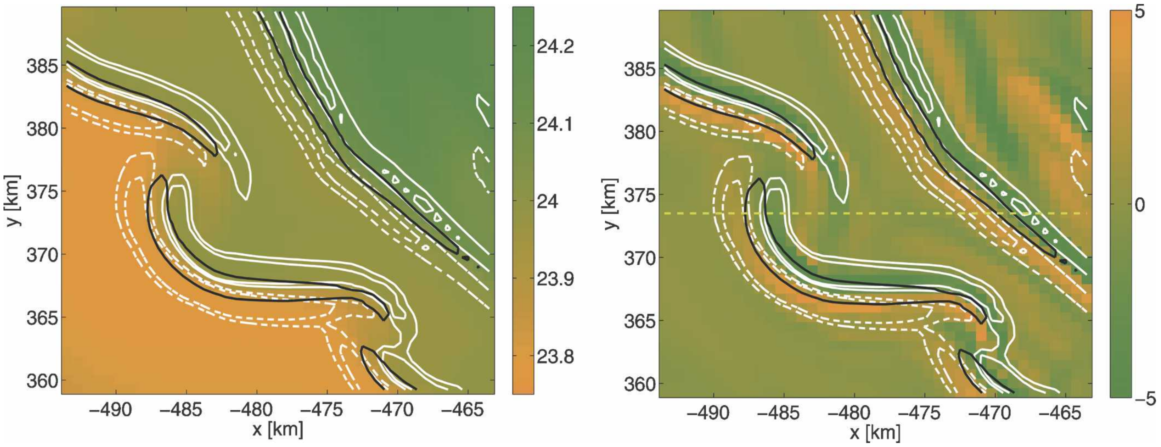

FIG. 5. Examples of frontal structure in ICC0: (left) $\rho(x, y)$ (kg m^{-3}–10^3) and (right) $w(x, y)$ (10^{-4} m s^{-1}) at 10-m depth in a (30 km)^2 subdomain. Contours are either $|\nabla_h \rho| = 1.2 \times 10^{-4}$ kg m^{-4} (solid black) or $\delta_2 = \pm 0.06$ and ± 0.1 kg m^{-3} (solid white for $\delta_2 > 0$; dashed white for $\delta_2 < 0$). The horizontal dashed line in the right-hand panel indicates the vertical section in Fig. 10.

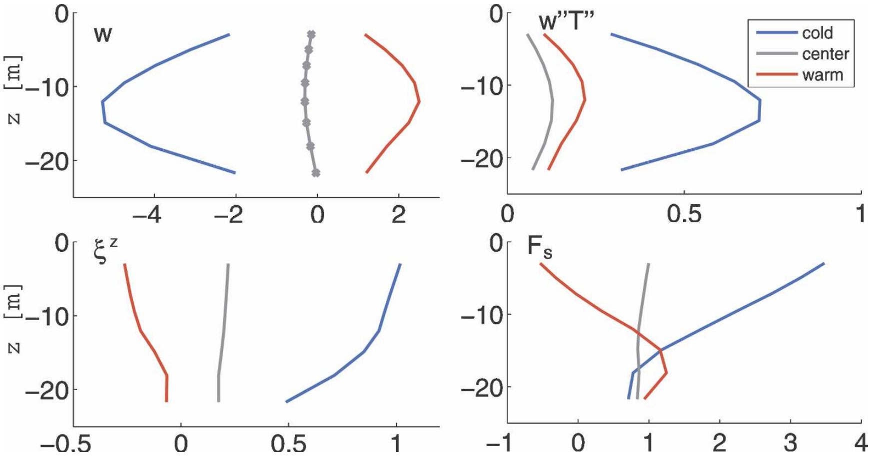

FIG. 6. Composite vertical profiles near fronts: w (10^{-4} m s^{-1}), $w''T''$ (10^{-4} m°C s^{-1}), ζ^z/f, and F_s (10^{-13} kg^2 m^{-8} s^{-1}). The designators (color; compositing criterion) indicate locations relative to the identified fronts: cold side (blue; $\delta_2 > 0.1$ kg m^{-3}), center (gray; $|\nabla_h \rho| > 10^{-4}$ kg m^{-4}), and warm side (red; $\delta_2 < -0.1$ kg m^{-3}). The dots superimposed on the gray line in the first panel show the vertical grid resolution. The mean boundary layer depths for the three composite regions are 16 (warm side), 25 (center), and 33 m (cold side).

stretching generation. Vertical heat flux is positive on both sides of the front and small in the center, but it is much stronger on the heavy side.[2] Last, the tendency F_s is generally positive and again strongest on the heavy side, where the surface horizontal ageostrophic flow is convergent. If the threshold value for $|\nabla_h \rho|$ is reduced, weaker fronts are included in the averaging, more cancellation occurs, and the signature of frontogenesis tends to fade. However, the frontogenesis patterns in Fig. 6 are still visible when the composite averaging is performed over the 10% grid cells having the strongest fronts; this remains true even when the 3% domain points making up Fig. 6 are excluded. Cold/warm-side compositings are somewhat more sensitive to their δ threshold value, but at least up to 1% of the domain can be included for each compositing without invalidating our previous description.

b. Frontogenetic mechanisms

Next we analyze the mechanisms inducing frontogenesis in ICC0. From the density equation, derived from the T and S equations while neglecting variations in the thermal expansion and haline contraction coefficients (appropriate to a local frontal analysis), the frontal tendency F (Giordani and Caniaux 2001) is

$$F = (\mathbf{Q}_{sg} + \mathbf{Q}_{sa} + \mathbf{Q}_{w} + \mathbf{Q}_{dv} + \mathbf{Q}_{dh}) \cdot \nabla_h \rho \equiv \Sigma_i \mathbf{Q}_i \cdot \nabla_h \rho. \tag{5}$$

The contributing vectors $\mathbf{Q}_{sg}$ and $\mathbf{Q}_{sa}$, defined as

$$\mathbf{Q}_{sg} = -(\partial_x u_g \partial_x \rho + \partial_x v_g \partial_y \rho, \partial_y u_g \partial_x \rho + \partial_y v_g \partial_y \rho) \quad \text{and} \tag{6}$$

$$\mathbf{Q}_{sa} = -(\partial_x u_a \partial_x \rho + \partial_x v_a \partial_y \rho, \partial_y u_a \partial_x \rho + \partial_y v_a \partial_y \rho), \tag{7}$$

represent straining deformation by, respectively, the geostrophic velocity, $\mathbf{u}_g = \hat{\mathbf{z}} \times (f\rho_o)^{-1} \nabla_h p$, and the ageostrophic horizontal velocity, $\mathbf{u}_a = \mathbf{u}_h - \mathbf{u}_g$. The vector

$$\mathbf{Q}_w = -\partial_z \rho \nabla_h w \tag{8}$$

is the analogous straining deformation by vertical velocity, and $\mathbf{Q}_{dv}$ is the diabatic term in the density equation due to the vertical mixing from the k-profile parameterization (KPP) scheme,

$$\mathbf{Q}_{dv} = \nabla_h (\partial_z \kappa \partial_z \rho). \tag{9}$$

The horizontal advection operator we used has an implicit horizontal diffusion (represented here by $\mathbf{Q}_{dh}$) that is difficult to diagnose in our solutions but is likely playing an important role in limiting the width of intense fronts (Shchepetkin and McWilliams 1998). We further define $F_i = \mathbf{Q}_i \cdot \nabla_h \rho$ for subscripts $i = \{sg, sa, w, dv, dh\}$.

Composite vertical profiles of the F_i components near fronts are shown in Fig. 7. The geostrophic straining term F_{sg} is positive, consistent with its role in frontal initiation; it is fairly uniform over the frontal region,

---

[2] For connection to the heat balance (section 7 of Part I), we also show the eddy vertical heat flux. In the surface boundary layer near fronts, the heat flux is essentially similar to the density flux, although there is some degree of T–S compensation in their separate contributions to ρ.

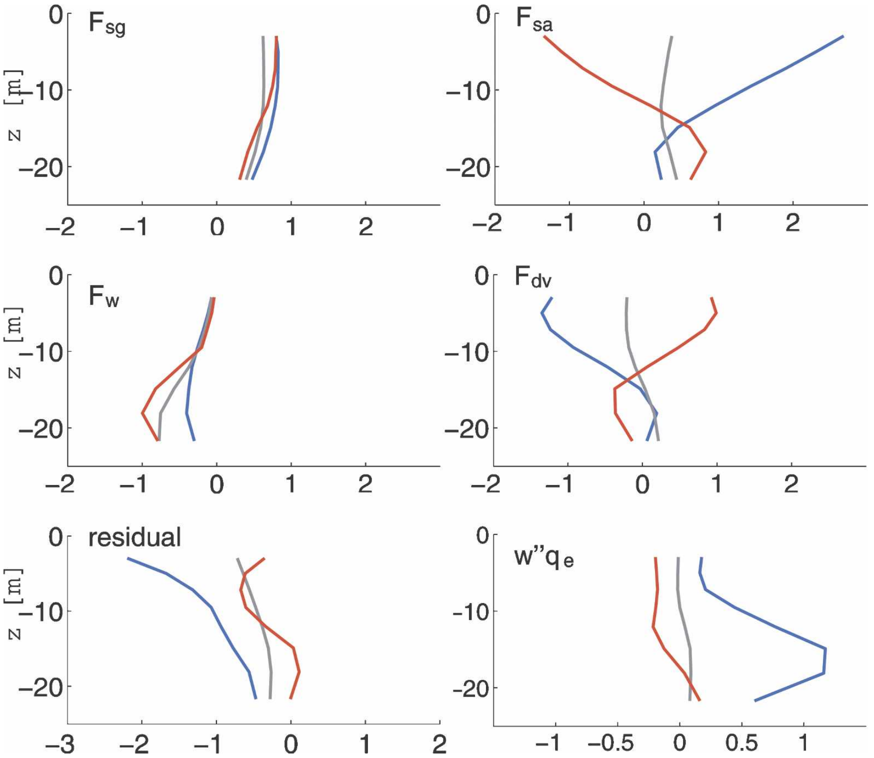

FIG. 7. Composite vertical profiles for the frontogenetic tendency terms defined in the text: F_{sg}, F_w, F_{dv}, and residual (10^{-13} kg^2 m^{-8} s^{-1}) for the heavy (blue), central (gray), and light (red) zones near the fronts. The final panel is a composite profile for submesoscale vertical potential vorticity flux, $w''q''$ (10^{-13} s^{-2}).

decreases only slowly with depth, and is relatively weak. In contrast, ageostrophic straining F_{sa} is stronger and more surface-intensified, and it acts asymmetrically to strengthen the front on its heavy side and weaken it on its light side. Near the surface F_{sa} is the dominant term, although its effect is weakened by the vertical mixing term F_{dv} with opposite sign. Vertical straining F_w weakens the front everywhere, especially on the light side, but with significant magnitude only below about 10-m depth (i.e., below where w is approaching its nearly zero surface boundary condition). The residual in (5), which is a mixture of front intensification and damping by horizontal diffusion, is also presented because we could not reliably compute either of these terms. [Because the composite is a conditional average based on the frontal intensity, the time tendency need not be zero in (2), e.g., if frontal collapse is faster on average than frontogenesis.]

3. Wind modulation of frontal dynamics

a. Wind-induced frontogenesis

In section 2b the frontogenetic influence of the wind-induced, nonlinear Ekman current (i.e., whose transport varies inversely with $f + \zeta^z$) is implicit in F_{sa} as part of the secondary circulation (Niiler 1969; Paduan and Niiler 1990; Thomas and Lee 2005; Thomas 2005). The wind influence is dependent upon the angle θ of frontal axis relative to the wind direction (Fig. 2), which determines whether its Ekman flow strengthens or opposes the frontal secondary circulation. Precisely, we define $\theta = \alpha\ \mathrm{acos}(\boldsymbol{\tau}\cdot\boldsymbol{\nabla}_h\rho/|\boldsymbol{\tau}\cdot\boldsymbol{\nabla}_h\rho|) + \pi(1/2 - \alpha)$, where $\alpha = \mathrm{sgn}[(\mathbf{z}\times\boldsymbol{\tau})\cdot\boldsymbol{\nabla}_h\rho]$. A composite analysis for the heavy side of fronts (i.e., the dynamically most active region; Fig. 6) is decomposed with respect to θ in Fig. 8. The vertical velocity and heat flux are strongest for a broad interval around $\theta \approx 0$ and weakest for $\theta \approx \pm\pi$. Thus, even in the diversely oriented family of fronts in our simulations (Fig. 3 herein or Figs. 4 and 5 of Part I), downwind fronts have more intense secondary circulation and restratification flux.[3] The heavy-side frontogenetic tendency F_s is large for small θ and weak for

---

[3] The mean surface density gradient in an upwelling system has the same wind orientation of $\theta \approx 0$. However, the mesoscale strain field is nearly isotropic in θ; hence, the result in Fig. 8 is mainly a manifestation of the wind effect on the submesoscale $\boldsymbol{\nabla}_h\rho''$, not on the mean $\boldsymbol{\nabla}_h\bar{\rho}$.

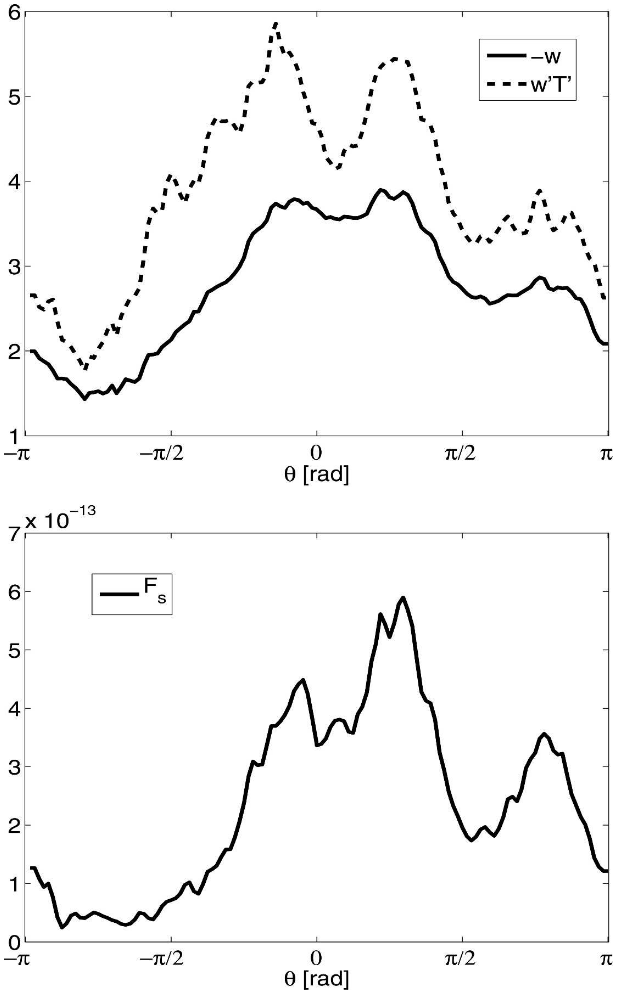

FIG. 8. Wind-angle dependence for composited frontal quantities on the cold/heavy side: (top) $-w$ (10^{-3} m s^{-1}) and $w''T''$ at 10-m depth (10^{-4}°C m s^{-1}), and (bottom) F_s (10^{-13} kg^2 m^{-8} s^{-1}) at 5-m depth.

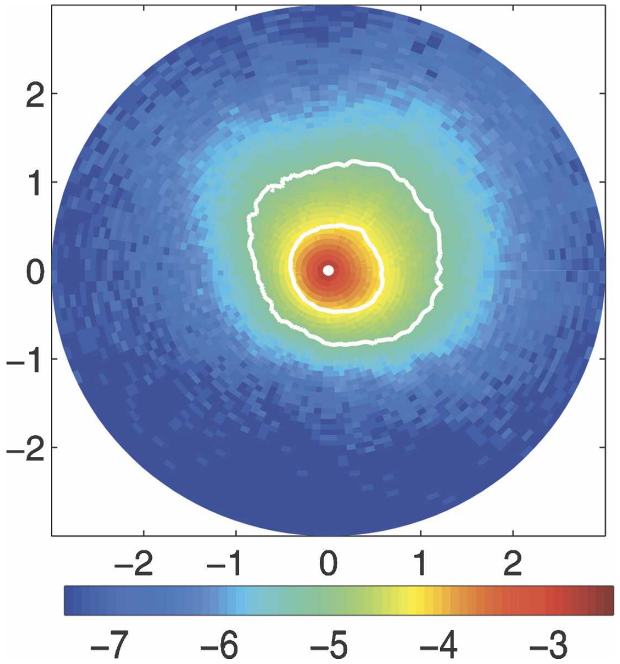

FIG. 9. Wind-angle dependence for the $|\nabla_h \rho|$ pdf in ICC0 at 5-m depth; θ is the azimuthal angle, and the radial distance on the plot represents $|\nabla_h \rho|$ (10^{-4} kg m^{-4}). The white lines correspond to pdf values equal to 10^{-4} and 10^{-5}.

$\theta \approx \pi$ (Fig. 8), mainly through F_{sa} (not shown); however, the extrema are slightly shifted from the values 0 and π, hence slightly differing from previous analytical solutions (Thomas and Lee 2005).[4] Note that, although the density gradient probability density function (pdf) bears this wind direction dependency, as can be readily seen in Fig. 9, the anisotropy is pronounced only for extreme fronts. A consequence is that the wind is a net source of energy for submesoscale fronts as a whole. It is unclear whether this frontal anisotropy could be observed in nature, where winds always have some degree of spatial (at the mesoscale and submesoscale) and temporal variability, notwithstanding sampling requirements.

b. *Potential vorticity and its frontal depletion*

Another nonlinear Ekman effect comes from the potential vorticity depletion that occurs at the front due to wind stress. In a rotating, stratified fluid the Ertel potential vorticity is defined by

$$q_e = -\frac{1}{\rho_o}(f\hat{\mathbf{z}} + \nabla \times \mathbf{u}) \cdot \nabla \rho. \tag{10}$$

Its governing equation (Müller 1995) is

$$\frac{Dq_e}{Dt} = -\frac{1}{\rho_o}(f\hat{\mathbf{z}} + \nabla_h \times \mathbf{u}) \cdot \nabla_h N_\rho - \frac{1}{\rho_o}(\nabla \times \mathbf{N_u}) \cdot \nabla \rho. \tag{11}$$

All vectors are fully three-dimensional; N_ρ is the diabatic term in the potential density equation, and $\mathbf{N_u}$ is the nonconservative force (including wind-induced friction). When the wind blows downfront, negative q_e is generated at the surface by the frictional torque $\nabla \times \mathbf{N_u}$ (mainly by the vertical shear $\partial_z \mathbf{u}_h$ multiplied by horizontal density gradient) (Thomas 2005).

---

[4] A possible explanation for this discrepancy is that Thomas and Lee's (2005) assumption of frontogenesis occurring uniformly over the whole depth of the Ekman layer is not accurate here since $\nabla_h \rho$ and F_s are concentrated in the upper part of the boundary layer (cf. Fig. 6). So, the strongest cross-front flow occurs for $\theta > 0$, where the near-surface Ekman spiral has rotated rightward from the wind direction less than the layer-averaged value for θ.

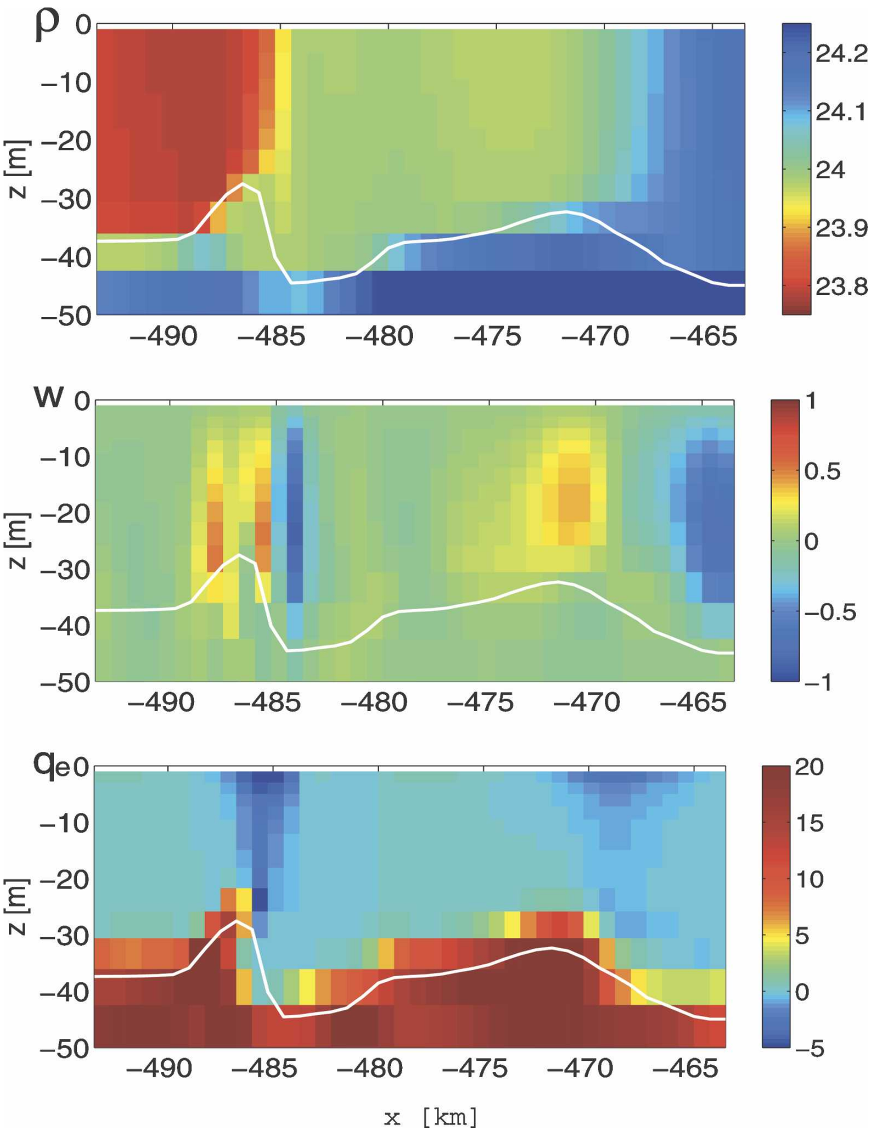

FIG. 10. Frontal cross sections for ρ (kg m^{-3} − 10^3), w (10^{-3} m s^{-1}), and q_e (10^{-10} m^{-1} s^{-1}) along the line indicated in Fig. 5. Note the nonlinear color bar for q_e. The depth of the boundary layer as computed by the mixing scheme (KPP) is represented as a white line on all panels.

The two fronts in Fig. 5 are aligned approximately downwind. Their vertical sections for ρ, w, and q_e are shown in Fig. 10. As expected from the weak stratification, q_e is small throughout the boundary layer, compared to the large positive values in the pycnocline, and it is clearly negative at the center of the fronts, especially near the surface, where the wind friction is expected to deplete potential vorticity. The downward branch of the secondary circulation advects negative potential vorticity toward the base of the boundary layer that tends to deepen (entrainment may also contribute to the deepening). Conversely, on the light side, the top of the high-q_e layer is pushed upward. In both cases, this implies an upward potential vorticity submesoscale eddy flux (i.e., $w''q''_e > 0$ in Fig. 7).

Triplets of polar plots representing composite q_e and $w''q''_e$ in the same three frontal subregions as in Fig. 6 confirm the statistical significance of potential vorticity depletion and vertical flux at the fronts. In every panel θ is the azimuthal angle, and the radial distance on the plot is an appropriate measure of frontal intensity: positive δ_2 on the heavy side, $|\nabla_h \rho|$ in midfront, and negative δ_2 on the light side (i.e., the same ones used in Fig. 6). We see in Fig. 11 that q_e near the surface is

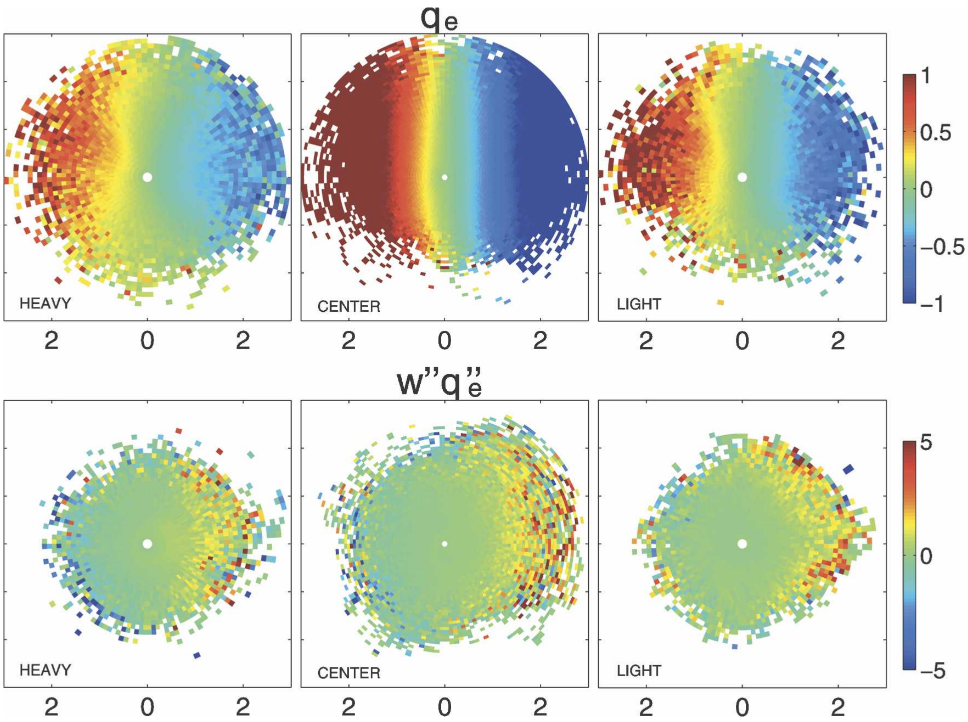

FIG. 11. Triplet polar plots for composited fields near surface fronts: (top) q_e at 5 m (10^{-9} m^{-1} s^{-1}) and (bottom) $w''q_e''$ at 20 m (10^{-13} s^{-2}) for the (left) heavy side, (middle) central region, and (right) light side, respectively (cf. Fig. 6). The units along the abscissa are for radial "distance" as the magnitude of the (left, right) local density anomaly (10^{-1} kg m^{-3}) or (middle) density gradient (10^{-4} kg m^{-4}). The azimuthal angle θ is the wind direction measured counterclockwise from downfront (Fig. 2).

directly related to θ, approximately varying as $\cos(\theta)$, with negative values for $-\pi/2 < \theta < \pi/2$. Except for $\theta \approx \pm(\pi/2)$, q_e increases in absolute value for increasing $|\nabla_h \rho|$, in agreement with (11). Where q_e is negative, $w''q_e''$ is positive within the boundary layer, which is also evident in its vertical profile (Fig. 7).

Thus, for those fronts with a roughly downwind alignment, the wind-induced effects on the primary strain-induced frontogenetic processes (Fig. 2) are an increased rate of frontogenesis, stronger secondary circulation, and generation of $q_e < 0$. The latter is conducive to centrifugal instability, but it is unclear how much of an influence this process has on the submesoscale instabilities manifested in our solutions (section 4). Thomas (2008) shows an evolution of wind-aided frontogenesis toward coherent vortex emergence through baroclinic instability.

4. Submesoscale instabilities

a. *Instability modes*

ICC0 exhibits a wide range of fluctuation scales in the alongfront direction, ranging from ~100-km mesoscale arcs to ~5-km submesoscale arabesques (Figs. 1 and 3). In many instances some form of submesoscale frontal instability with wavelength between 10 and 30 km is responsible for breaking the alongfront regularity. Figure 5, in particular, shows an apparently unstable front that has developed strong submesoscale meanders, alongside another front that is still straight, hence apparently stable at this time. Without such instability there would not be as much submesoscale scalloping of the surface ρ gradients (Fig. 3 herein and Fig. 4 of Part I), nor fragmentation of the ζ^z filaments leading to submesoscale vortices (Fig. 5 of Part I).

Provided that submesoscale frontal flows can be considered in isolation and idealized as surface-intensified parallel flows (as in Fig. 2), several modes of linear, normal-mode instability are potentially relevant to the ICCO simulation (McCreary et al. 1991; Samelson 1993; Wang 1993; Samelson and Chapman 1995; Barth 1994; Spall 1995; Haine and Marshall 1998; Nurser and Zhang 2000; Boccaletti et al. 2007). Of course, this idealization ignores the effects of mesoscale straining and secondary circulation in active frontogenesis, as well as finite-time and finite-amplitude aspects of fluctuation growth. Larger-scale straining, in particular, can suppress horizontal shear instability for a vorticity filament in a barotropic flow (Moore and Saffman 1975; Dritschel et al. 1991). So far, relatively little is known about the more general competition between instability and active frontogenesis in a baroclinic flow, although Spall (1997) and Bishop (1993) generally see reduced instability with straining.

In quasigeostrophic theory, as well as in more general dynamical regimes, a normal-mode instability of a parallel shear flow can arise if there is a change in sign of the horizontal gradient of potential vorticity (Pedlosky 1987). This is commonly referred to as barotropic instability when the dominant sign change is associated with horizontal shear or as baroclinic instability when it is mainly due to vertical shear. This necessary condition is manifestly satisfied in Fig. 10. Horizontal gradients become quite large through frontogenesis, and both upwelling filaments and fronts have large vertical shear near the base of the boundary layer. Both shear-instability types can lead to downflow meanders and coherent vortices at finite amplitude. For finite Rossby and Froude numbers, ageostrophic instabilities have been found in several different flow configurations (Stone 1966b; Barth 1994; McWilliams and Yavneh 1998; Molemaker et al. 2001 2005), especially in anticyclonic regimes. This instability type favors somewhat smaller scales than the quasigeostrophic instability types when both can occur, and it develops with an "unbalanced" velocity field (section 5). For flows with $O(1)$ Rossby and Froude numbers (e.g., $|\zeta^z/f| > 1$ in Fig. 5 of Part I) and a change in sign of q_e itself (Fig. 10), centrifugal instability can occur (Hoskins 1974; Haine and Marshall 1998). This type can be, though not necessarily, symmetric in the downflow direction; if so, then it would be part of the secondary circulation that in principle is distinct from the frontogenetic part but in practice might be difficult to distinguish. Finally, for even larger Rossby and Froude numbers, microscale instabilities—for example, Kelvin–Helmholtz instability ($|d\mathbf{u}_h/dz|$ that is large relative to the stratification strength) or convection ($d\rho/dz > 0$)—can occur. Careful examination of the simulation fields has revealed no sign of Kelvin–Helmholtz instability and only a handful of convective instabilities (section 5). We attribute this to the anisotropic horizontal and vertical grid resolution in our simulations because conditions conducive to both instabilities are widely present in the boundary layer, especially in the vicinity of fronts. We first focus on instabilities with the shortest wavelengths (10–20 km, only marginally outside the kinetic energy dissipation range; Fig. 6 of Part I), for which we are able to perform a clean mean-eddy decomposition and hence accurately compute local energy transfer terms. Possible instabilities at somewhat larger scales (but yet below the mesoscale) are then considered.

b. *Instability case studies*

We investigate the character of the submesoscale frontal instability for three quasi-rectilinear frontal destabilization events. We compute the kinetic energy conversion terms between the parallel (frontal) flow and its meandering perturbations (Harrison and Robinson 1978) in a local reference frame with its x_* axis aligned with the main front. Our analysis method is almost comprehensive in its possible conversion terms for perturbation kinetic energy,[5] but we do not examine the local energy transport terms (which would be zero if there were local horizontal homogeneity). The local coordinates are x_* and y_* in the along- and cross-front direction, respectively, with horizontal velocities u_* and υ_* (Fig. 2). For this analysis the local mean, denoted by angle brackets, is defined as the alongfront average for the region considered. Perturbations relative to that mean are denoted with a caret. We also remove the alongfront trends from the perturbations, assuring that $\langle \partial_{x_*} \hat{\cdot} \rangle = 0$. Assuming that the local regions considered are of sufficient extent in the x_* direction to contain a few wavelengths of the frontal instability, any nonzero, alongfront trend is part of the background mesoscale flow rather than the local submesoscale instability.

The integrand in the area-integrated rate of conversion from mean to perturbation kinetic energy is defined by

$$K_mK_e = \frac{1}{\eta - z_0}\int_{z_0}^{\eta} (-\langle \hat{u}_*\hat{\upsilon}_*\rangle \partial_{y_*}\langle u_*\rangle - \langle \hat{u}_*\hat{w}\rangle \partial_z \langle u_*\rangle)\, dz,$$

$$\equiv K_mK_e^h + K_mK_e^\upsilon, \tag{12}$$

where a partial depth average is also performed between an interior level $z_0 < 0$ and the sea surface height η. The first of the two right-hand-side terms will be denoted by $K_mK_e^h$, and it arises from the product of horizontal mean shear and Reynolds stress. The second right-hand-side term, denoted by $K_mK_e^\upsilon$, arises from vertical shear of the mean flow and vertical Reynolds stress. The analogous perturbation potential to kinetic energy conversion is

---

[5] The kinetic energy conversion associated with symmetric perturbations (i.e., uniform along the front) is not examined by our technique because we do not distinguish between a stationary background symmetric frontal flow and an evolving one. This limits our ability to draw conclusions about the occurrence of centrifugal instability in its symmetric mode. Note that negative q_e regions are present in the vicinity of the frontal cases 1 (Fig. 12a) and 3 (Fig. 13).

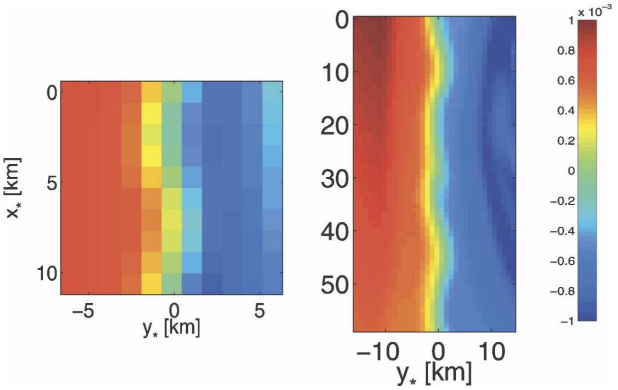

FIG. 12. Submesoscale instability: local subdomains for surface buoyancy anomaly b (10^{-3} m s^{-2}) for the frontal cases (left) 1 and (right) 2. Each plot has a true aspect ratio, but the absolute length scale varies between the plots. The horizontal coordinates (x_*, y_*) are rotated to align with the front (cf. Fig. 2).

$$PK_e = \frac{1}{\eta - z_0}\int_{z_0}^{\eta} \langle \hat{w}\hat{b}\rangle \, dz, \tag{13}$$

where b is the buoyancy anomaly relative to the local area average (i.e., the density anomaly times $-g/\rho_0$, where ρ_0 is the reference density equal to 1000 kg m^{-3}). For an indication of the mesoscale straining and frontogenetic effect averaged along the front, we also compute a local mean potential-to-kinetic energy conversion,

$$PK_m = \frac{1}{\eta - z_0}\int_{z_0}^{\eta} \langle w\rangle\langle b\rangle \, dz, \tag{14}$$

that is a source for the mean frontal flow. In all of the cases that we considered, PK_m is the dominant conversion term, by an order of magnitude or more in cases 1 and 3. This is presumably a consequence of our methodological requirement for quasi-rectilinear fronts: when the instability does arise in the presence of significant strain rate, it may only occur for a limited high-wavenumber set (Bishop 1993; Spall 1997), that is, lead to a cleanly decomposable flow.

We choose z_0 approximately equal to the boundary layer depth, so these energy conversions are approximately boundary layer averages. We have checked that the contributions from below the surface layer are negligible, confirming that both the frontogenetic process and submesoscale instabilities are mainly confined to the surface boundary layer. Note, however, that since the vertical integration has an open lower boundary, the pressure work and vertical energy advective flux may give nonzero contributions, but in practice this term is small in our solutions.

Growing wave patterns are visible in Fig. 12 for cases 1 and 2 and in Fig. 13 for case 3. For case 3 the decomposed mean and perturbation fields are shown for u_*, v_*, and w in Fig. 15, below. The energy conversion results are in Fig. 14. The value of PK_e is always positive, and it is the dominant source of energy for the perturbation in all cases. The vertical Reynolds stress ($K_mK_e^v$) is variable from case to case, sometimes positive and about ¼ the amplitude of PK_e (case 2) and sometimes negligible (cases 1 and 3). It is always largest in the lowest 10 m of the boundary layer, where the mean vertical shear is largest. Averaged over the boundary layer, the horizontal Reynolds stress ($K_mK_e^h$) is never the dominant conversion, but it is positive in depth average in case 1 and is comparable to PK_e in the upper 10 m (not shown). This suggests that the horizontal and vertical shear of the mean frontal flow is not essential to the development of the observed submesoscale frontal instabilities, though it may be a contributing element. Three additional cases (not shown) were analyzed to confirm this, and none had a significant K_mK_e conversion. This is consistent with previous linear instability for upper-ocean frontal jets, where $PK_e > 0$ is the primary conversion term, and even very narrow frontal jets show only weak $K_mK_e^h > 0$ conversion, except when centrifugal instability sets in (Barth 1994). In cases 1 and 3 there is some occurrence of $\langle q_e\rangle < 0$ (section 3b) but not in case 2; however, in none of these cases is there dominance of $K_mK_e > 0$ conversion, indicating that centrifugal instability is not the source of the meanders seen in Fig. 12.

Because these instabilities are mostly confined within the boundary layer, we follow Boccaletti et al. (2007; see also Hosegood et al. 2006) and compute a "mixed layer" deformation radius R_{ml}, adapted for our situation where the boundary layer is most often completely mixed or even unstably stratified with increased stratification toward its base. We define $R_{\mathrm{ml}} = (\Delta B h_{\mathrm{bl}})^{1/2}/f_0$, with h_{bl} as the depth at which the density exceeds the surface value by 0.02 kg m^{-3} and ΔB as the difference between the surface buoyancy and the buoyancy at the grid point immediately below h_{bl}; R_{ml} values computed in this way are quite spatially variable but remain in the range 2–4 km in the regions where our case study instabilities unfold.[6] We will come back to this point in section 7, but this hints at the similarity between the mixed layer instability found by R. Ferrari et al. (2007, personal communication) and us. In the remainder of the paper the term mixed layer submesoscale instabilities (MLSI) will be used to refer to the submesoscale instabilities with wavelength <20 km and approximate

---

[6] A nearshore average R_{ml} value is around 1 km (where our horizontal resolution is inadequate to any associated mixed-layer instabilities), and offshore values as large as 10 km can be found.

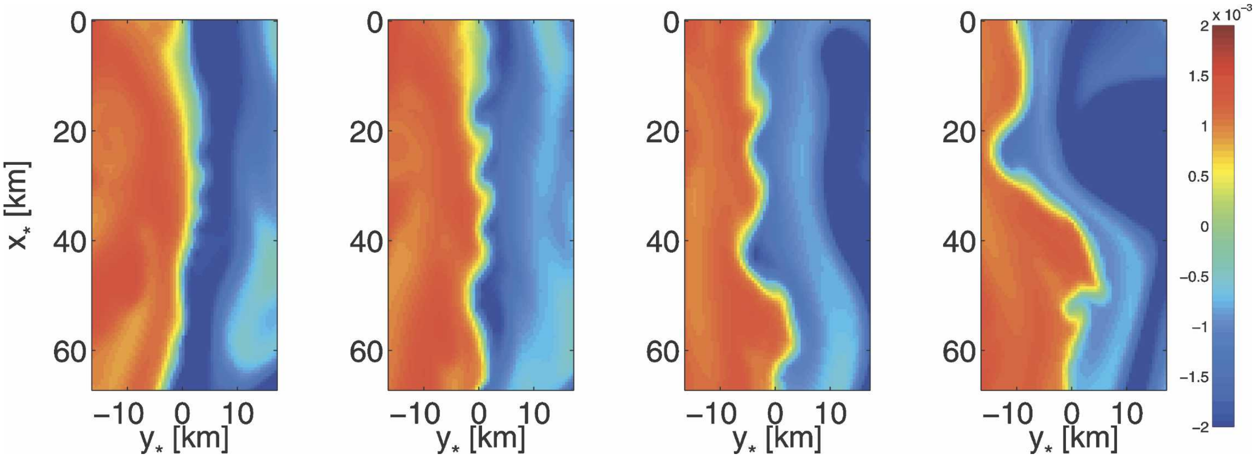

FIG. 13. Submesoscale instability: local subdomains for surface b anomaly (10^{-3} m s^{-2}), relative to the local area average, for the frontal case 3 at successive times 1 day apart starting at $t = 207$ days. Meander growth is evident. The horizontal coordinates (x_*, y_*) are rotated to align with the front (cf. Fig. 2) at day $t = 208$ days (second panel from left) when the local energy transfer terms are computed. The front at $t = 208$ days can be seen in Fig. 1 around ($x = -250$ km, $y = 350$ km).

confinement within the boundary layer, analogous to those just described. In all cases shown here, the MLSI do not simply distort the ambient straining field and frontogenetic patterns but also put their own imprint on them. For example, $w(x, y)$ in Fig. 15 (see also Fig. 20a) reproduces the similar patterns as for mesoscale baroclinic instability (Hoskins and West 1979). In other words, even though their wavelengths are quite far down the submesoscale range, restoration of thermal wind balance (i.e., a mechanism that underlies frontogenesis) remains an important constraint for the flow associated with submesoscale instabilities.

c. *Submesoscale turbulence*

Satellite images reveal instances of clear submesoscale destabilization (Fig. 16) events such as the ones we have analyzed. In nature, as in our solutions, the most conspicuous signs of instability seem to be at scales somewhat larger than 10–20 km, although that may partly be an observational bias from the limited resolution in satellite images. Examples of such signs can be seen in Fig. 3 around $y = 450$ km and -400 km $< x < -250$ km, as well as along the edges of the offshore mesoscale eddies in Fig. 1. Unfortunately, the eddy-mean decomposition technique is hopeless for these features because they coexist with and strongly participate in a complex submesoscale turbulent flow and are rarely in a stage resembling linearly unstable growth.

In Fig. 17 we attempt to discredit the possibility of an intrapycnocline baroclinic instability with a small vertical scale perhaps close to a higher baroclinic mode (e.g., with $R_2 \approx 15$ km or $R_3 \approx 10$ km, hence a fluctuation wavelength around 60–90 km). We represent potential vorticity q_e and isopycnals along a section at $x = -400$

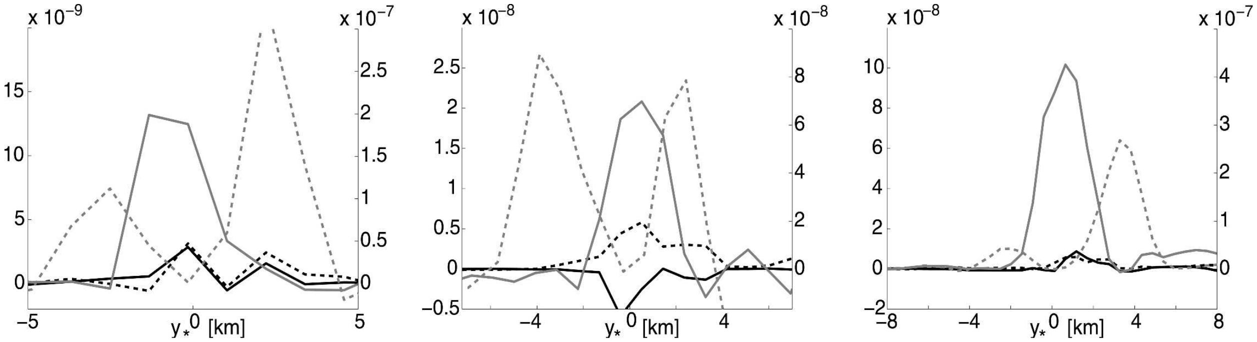

FIG. 14. Instantaneous local energy conversion profiles (averaged along the front) in submesoscale instability events, $\langle PK_e \rangle$ (solid gray), $\langle K_m K_e^h \rangle$ (solid black), $\langle K_m K_e^v \rangle$ (dashed black), and $\langle PK_m \rangle$ (dashed gray) (m^2 s^{-3}), for (left) case 1, (center) case 2, and (right) case 3. The right ordinate refers only to PK_m, and the left ordinate refers to all other conversions.

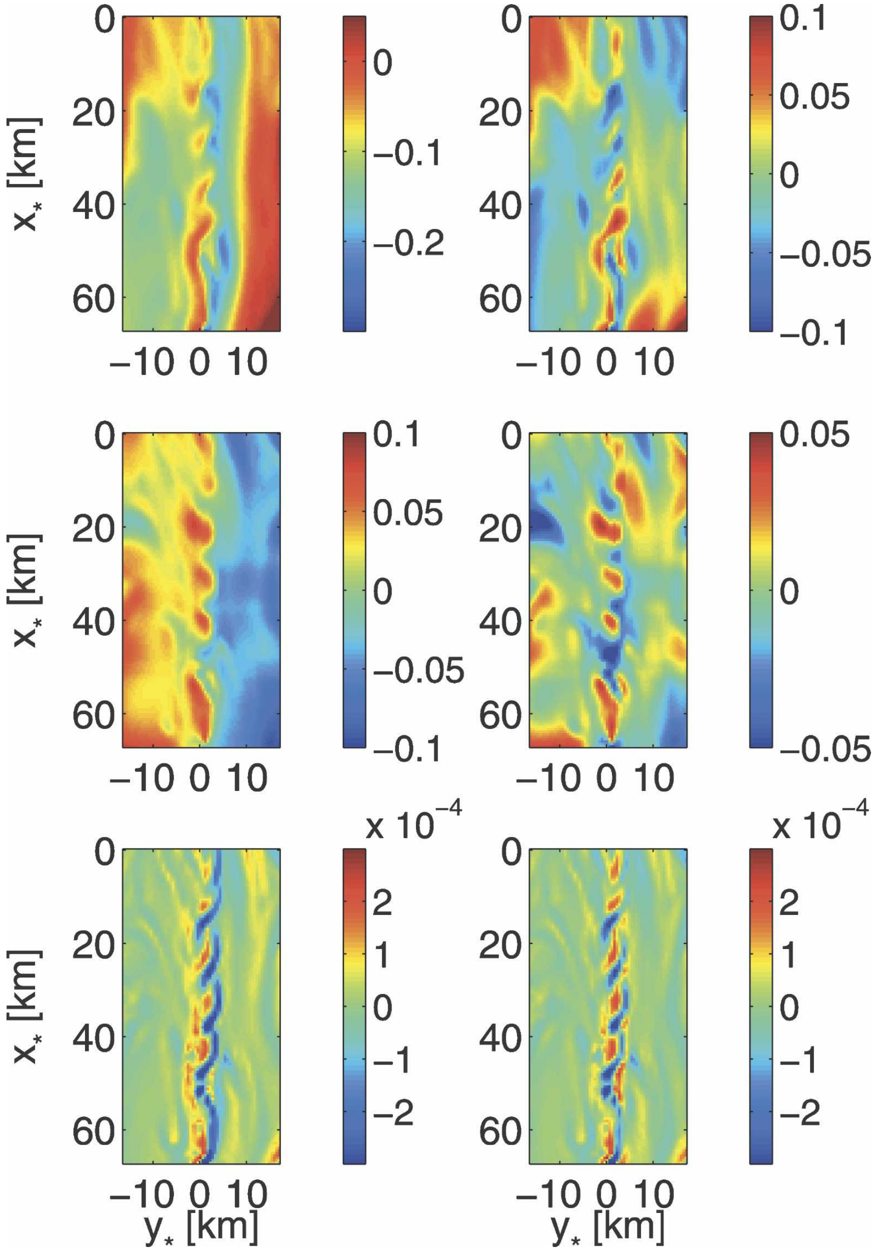

FIG. 15. (left) Total and (right) perturbation velocity components (m s^{-1}) for case 3 (Fig. 12): (top) alongfront u_*, (middle) cross-front v_*, and (bottom) vertical w.

km in Fig. 1. The q contours follow very closely the isopycnals below 200-m depth. More precisely, potential vorticity anomalies associated with the mesoscale isopycnal displacements domings are concentrated near the upper surface, with no sign of reversal deeper within the pycnocline. Therefore, there is no obvious violation of the Charney–Stern condition for stability (Pedlosky 1987), in particular in the vicinity of the major fronts at y = 200 and 350 km, where the string of submesoscale meanders can be seen. This argues against the occurrence of a finescale, intrapycnocline baroclinic instability, although neither does it rigorously disprove it.

Ageostrophic anticyclonic instabilities supported by the near-surface fronts on horizontal scales of tens of kilometers and down to depths of 50–100 m (Narimousa and Maxworthy 1985; Barth 1994; Eldevik 2002) (Fig. 17) are likely possibilities, as are more balanced baroclinic instabilities associated with boundary layer vertical shear and weak stratification (Haine and Marshall 1998; Boccaletti et al. 2007).

In interpreting the evident instability scale that is of-

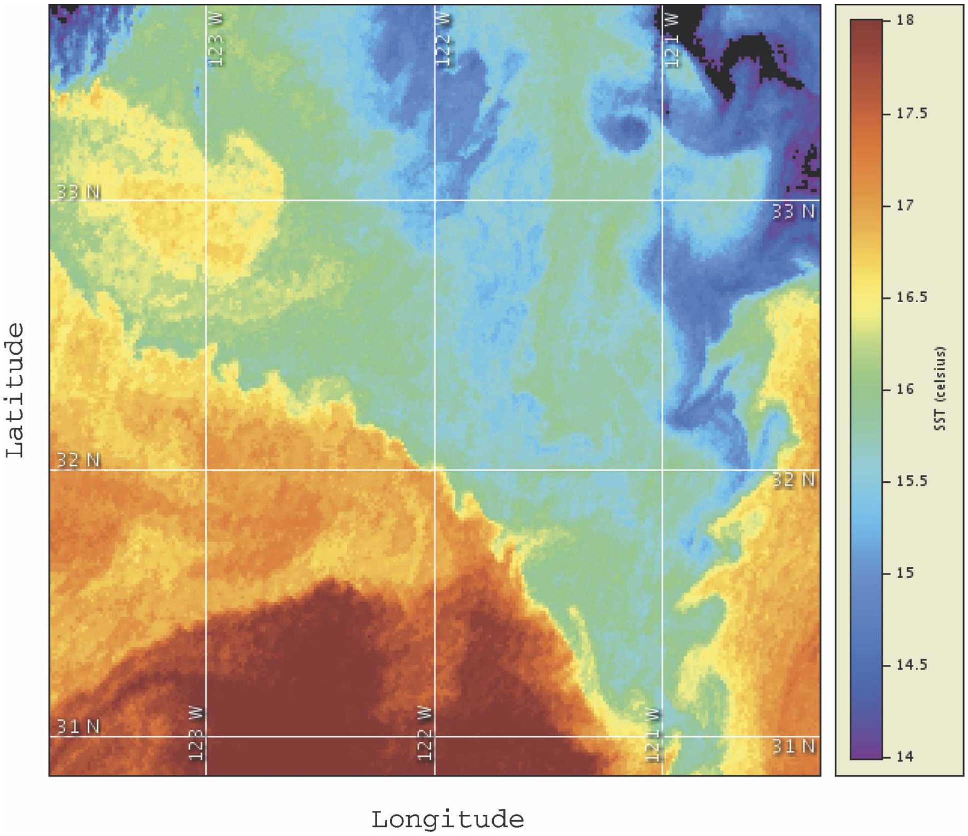

FIG. 16. Sea surface temperature measured at 1832 UTC 3 Jun 2006 off Point Conception in the California Current from CoastWatch (http://coastwatch.pfeg.noaa.gov). The fronts between recently upwelled water (i.e., 15°–16°C) and offshore water (≥17°C) show submesoscale instabilities with wavelengths around 30 km (right front) or 15 km (left front). Images for 1 day earlier and 4 days later show persistence of the instability events.

ten larger than R_{ml}, we also note that one effect of ambient strain whose extensional axis coincides with the frontal axis is to elongate the alongfront scale of an amplifying fluctuation compared to its preferred scale without strain (Bishop 1993). An evolutionary increase in the alongfront scale is evident in Fig. 13. Therefore, even if R_{ml} is smaller than the evident instability scale and fluctuations are sometimes seen below the boundary layer (down to 100 m in Fig. 17), it is still plausible that MLSI is a key process for generating submesoscale activity over a wide range of scales. In that regard, a comparison between our simulations ICC0 and ICC1 and the solution analyzed by Klein et al. (2008) at a similar grid resolution is instructive. In both solutions the flow develops intense fronts with $O(1)$ Rossby and Froude numbers. However, the solution of Klein et al. exhibits vorticity fields organized as gently curved filaments that are continuous over distances of tens or even hundreds of kilometers. In contrast, vorticity filaments in ICC0 and ICC1 are heavily wrinkled and broken into submesoscale fragments—that is, are unstable on the submesoscale. The two problem posings are different in several ways, including the mean stratification (i.e., a shallow eastern boundary current versus a deep profile representative of the Antarctic Circumpolar Current and no surface mixed layer). The latter suggests that surface frontal stability may be importantly influenced by surface stratification, with a mixed layer and associated small R_{ml} being more conducive to MLSI.

5. Diagnostic force balance

An important dynamical issue for submesoscale flows is the degree to which they satisfy a diagnostic horizontal force balance, either geostrophic balance (in which Coriolis and pressure-gradient forces are dominant) or the more general gradient-wind balance (in which these two forces plus an advective centrifugal force dominate the divergence of the horizontal momentum balance) expressed as (McWilliams 1985)

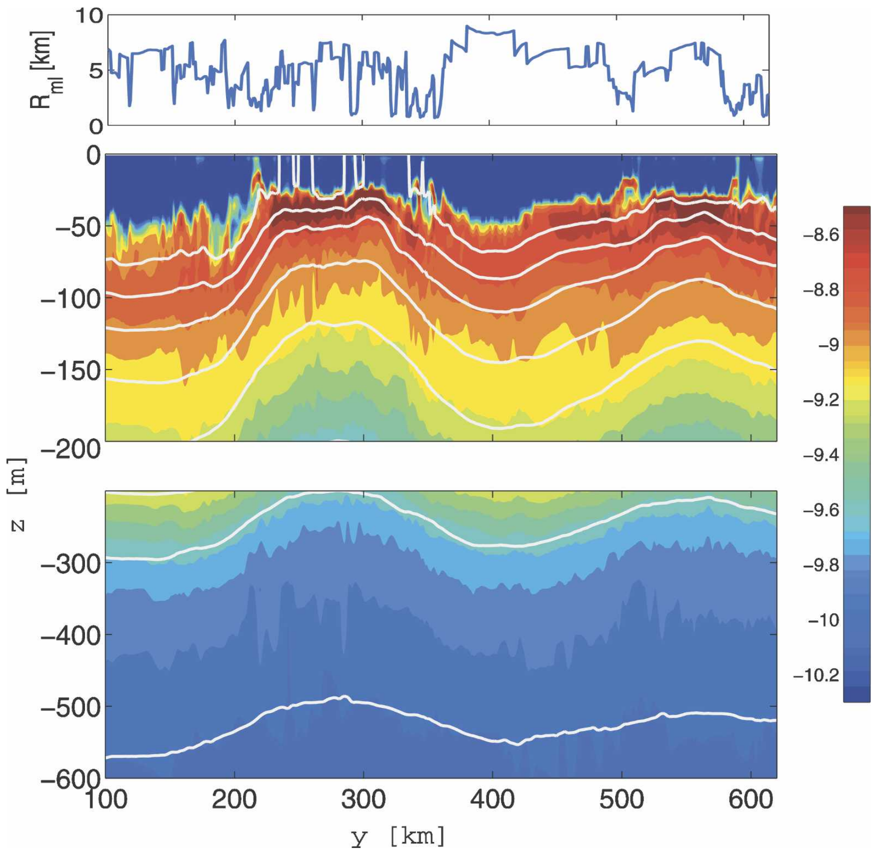

FIG. 17. Cross section of (top) R_{ml} (km) and (middle, bottom) q_e ($\mathrm{m}^{-1}\ \mathrm{s}^{-1}$) with a logarithmic scale with isopycnals superimposed (white lines). Note the different vertical scales for the lower panels.

$$-\boldsymbol{\nabla}_h \cdot (\mathbf{u}_h \cdot \boldsymbol{\nabla}_h \mathbf{u}_h) + f\zeta^z = \frac{1}{\rho}\nabla_h^2 p. \tag{15}$$

We assess the degree of diagnostic force unbalance in our solutions on the departure from (15) after a suitable normalization to provide a relative measure,

$$\epsilon_{\mathrm{gw}}(\mathbf{x}, t) = \frac{\left|-\boldsymbol{\nabla}_h \cdot (\mathbf{u}_h \cdot \boldsymbol{\nabla}_h \mathbf{u}_h) + f\zeta^z - \frac{1}{\rho}\nabla_h^2 p\right|}{|\boldsymbol{\nabla}_h \cdot (\mathbf{u}_h \cdot \boldsymbol{\nabla}_h \mathbf{u}_h)| + f|\zeta^z| + \left|\frac{1}{\rho}\nabla_h^2 p\right| + \mu}. \tag{16}$$

Here, $\mu = f\zeta^z_{\mathrm{RMS}} + \rho^{-1}(\nabla_h^2 p)_{\mathrm{RMS}}$ is added to the denominator of (16) to exclude situations with locally weak force divergences from being identified as significantly unbalanced. The degree of unbalance thus lies between $\epsilon = 0$, fully balanced, and $\epsilon \approx 1$, fully unbalanced. An analogous, less restrictive, unbalance measure based on geostrophic balance is

$$\epsilon_{\mathrm{geo}}(\mathbf{x}, t) = \frac{\left|f\zeta^z - \frac{1}{\rho}\nabla_h^2 p\right|}{f|\zeta^z| + \left|\frac{1}{\rho}\nabla_h^2 p\right| + \mu}, \tag{17}$$

but it fails to recognize submesoscale vortices as balanced because the curvature effects in the velocity field are important at such scales [as included in (16)].

Performing this unbalance analysis on our solutions shows that the mesoscale flow is highly geostrophically balanced, and even the near-surface submesoscale flow is mostly well balanced; this is shown by a decomposition of the kinetic energy spectrum in section 4 of Part III. In Fig. 18, ϵ_{geo} and ϵ_{gw} are shown for a 50 km × 50 km ICC0 subregion surrounding a submesoscale vortex. Their most noticeable difference is the much higher degree of balance in the vortex with the gradient-wind measure compared to the geostrophic. This is because the curvature effects in the velocity field are important at the submesoscale, and ignoring them leads to large errors in the assessed unbalance.

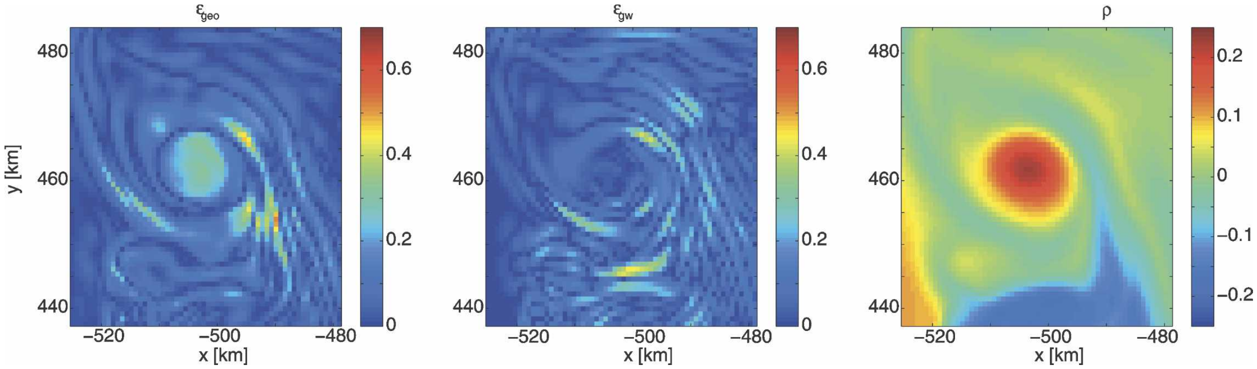

FIG. 18. Relative error in (left) geostrophic balance ϵ_{geo} and (middle) gradient-wind balance ϵ_{gw} at the surface in a (48 km)^2 subdomain around a submesoscale vortex. (right) The corresponding $\delta\rho$ anomaly (10^{-1} kg m^{-3}) is also shown. The vortex is approximately in gradient-wind balance with a significant cyclostrophic force divergence.

However, even the more conservative estimate based on (16) indicates several areas with significant unbalance that coincide with the strong density gradients [e.g., Figs. 18 (middle) and 19]. The ϵ_{gw} patterns roughly resemble those of other frontally intensified quantities such as w or F_s in Figs. 3 and 4. There is some degree of stripiness in the ϵ_{gw} patterns, as is also evident in other frontal quantities, especially w. Because of the large degree of unbalance, the possible involvement of inertia–gravity waves was investigated by examining animations of the ICC0 fields at 10-min intervals. No movement of the unbalanced areas distinct from advective displacements by the local velocity was found in the surface layer (e.g., unbalanced stripes move in the same manner as do the patterns in ρ). This contrasts with spontaneous gravity wave emission by tropopause jet streaks in the atmosphere (Zhang 2004).[7]

In more general terms, the submesoscale flow can exhibit locally significant unbalanced behavior, either by essentially balanced processes (e.g., baroclinic instability) that develop $O(1)$ Rossby number and ϵ_{gw} or by processes that simply have no balanced equivalent (e.g., ageostrophic instability; Barth 1994; Molemaker et al. 2005). Figure 20 shows ϵ_{gw}, $\partial_z w$, and F_s (an indicator for the frontogenesis induced by straining) for three situations with relatively simple submesoscale flow patterns. One (top row) is a baroclinic instability with significant unbalance occurring simultaneously with continuing frontogenesis, albeit somewhat fragmented by the instability. The second case is strong frontogenesis with significant unbalance in the secondary circulation but no development of a submesoscale instability in its evolution. The third case is a relatively rare example of convective instability with unstable stratification that persisted over several days despite the parameterized vertical mixing within the boundary layer; it is highly unbalanced, and it has no organized frontogenetic tendency.[8] From these examples we conclude that the most prevalent unbalance is associated with ageostrophic circulation induced by frontogenesis. Both frontal cases in Fig. 20 show a high correlation between ϵ_{gw} and F_s. This relationship can be inferred more generally by comparing ϵ_{gw} in Fig. 19 and F_s in Fig. 3. In particular, the MLSI in Fig. 20, as well as the other ones considered in section 4, do not appear to possess a grossly different type of unbalance than found in frontogenesis, although it is modulated along an unstable front as part of the MLSI.

6. Surface dynamics as an approximate submesoscale model

An important interpretive framework for the results presented here and in Part I is force-balanced surface dynamics (Blumen 1978; Held et al. 1995). Its dynamical approximations are uniform potential vorticity q_e in the interior, a surface density field $\Theta = \rho(x, y, 0, t)$ advected by a horizontal velocity field determined from q_e and Θ through the constraint of diagnostic force balance (section 5), and vanishing flow far from the bound-

---

[7] Below the boundary layer in a sequence of vertical sections for w, we found at least one instance suggestive of finescale, downward wave radiation away from a surface-layer front, with the pattern phase locked relative to the front (cf. O'Sullivan and Dunkerton 1995; Plougonven and Snyder 2007). A better-resolved simulation would be needed to investigate this further.

[8] Convection is a process for which we expect important nonhydrostatic effects that are excluded from our hydrostatic model. Nevertheless, hydrostatic convection has the same essential cause from the potential energy of unstable stratification.

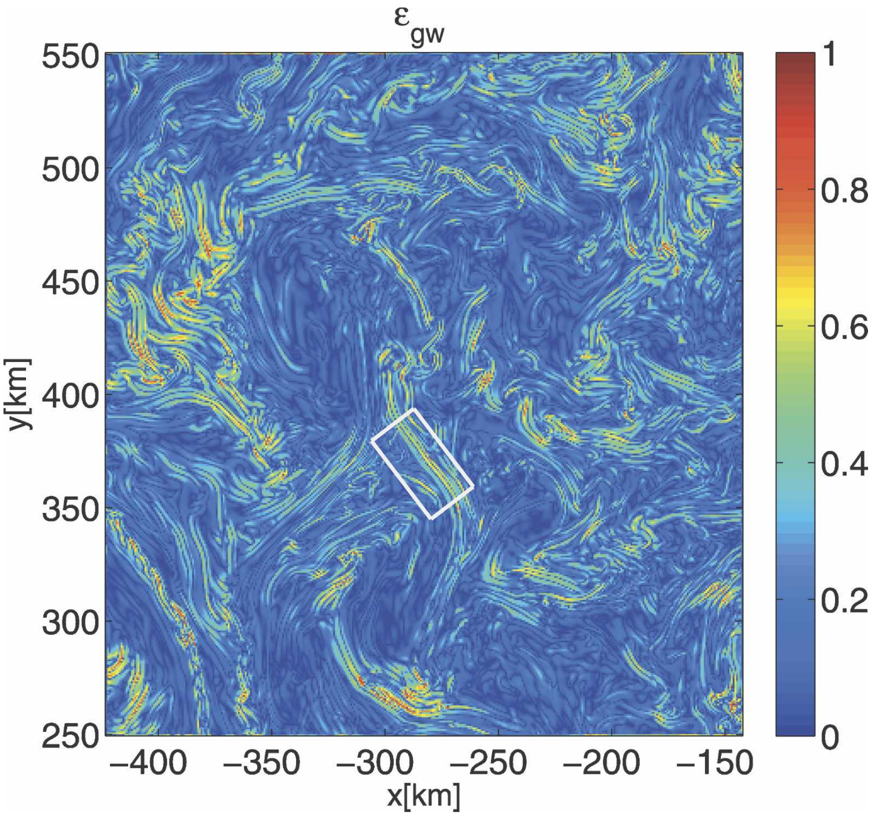

FIG. 19. Relative error in gradient-wind balance ϵ_{gw} at the surface for the same large subdomain plotted in Fig. 3. Frontal regions exhibit significant unbalance. The white box indicates the particular frontal region plotted in the middle row of Fig. 20.

ary. Heuristic plausibility arguments for the relevance of surface dynamics are the strong surface T gradients and weak variations of q_e in the upper ocean (Fig. 4 of Part I and Fig. 10 herein). Even with geostrophic balance (i.e., surface quasigeostrophy), surface dynamics exhibits many of the qualitative behaviors we see in the submesoscale transition in our simulations [as well as in previous ones by Lapeyre and Klein (2006)]: energization of the submesoscale, shallow horizontal spectrum slopes for velocity and tracers (Blumen 1978; Pierrehumbert et al. 1994), active frontogenesis in Θ, and generation of filaments and vortices (Juckes 1995) in $\zeta^z(x, y, 0, t)$. On the other hand, the assumptions for surface dynamics are obviously strong simplifications relative to our simulations with boundary layer mixing; q_e variations, especially in the pycnocline; ageostrophic straining during frontogenesis (Fig. 7); and violations of diagnostic force balance. The strongest qualitative discrepancy is that an isolated, parallel density front is linearly stable in surface quasigeostrophy (Held et al. 1995); that is, a baroclinic instability is suppressed. Thus, submesoscale fronts in surface quasigeostrophic turbulence retain large alongfront scales whose orientation is organized by the mesoscale circulation (cf., Fig. 10 of Held et al. 1995 and Fig. 16 of Celani et al. 2004).

Some useful generalizations of surface quasigeostrophy can be made. R. Ferrari et al. (2007, personal communication) recently combined a shallow, weakly stratified layer with a surface quasigeostrophic "interior" dynamics that leads to widespread submesoscale geostrophic instability sharing many characteristics with the MLSI in our simulations. Last, with a generalization of the diagnostic force-balance relation for finite Rossby number, surface dynamics also exhibits a dominance of cyclonic ζ^z near the surface (Hakim et al. 2002; their Fig. 5), which also occurs in our simulations (section 5). Nevertheless, the intermittent occurrence of a large degree of unbalance (section 5 of Part 1) makes it clear that surface dynamics is not a complete paradigm for the submesoscale frontal dynamics in ICC0. Similarly, Mahadevan and Tandon (2006) show with a simulation of an unstable surface front that its vigorous submesoscale w field corresponds only roughly to a balanced diagnostic analysis (i.e., an Ω equation).

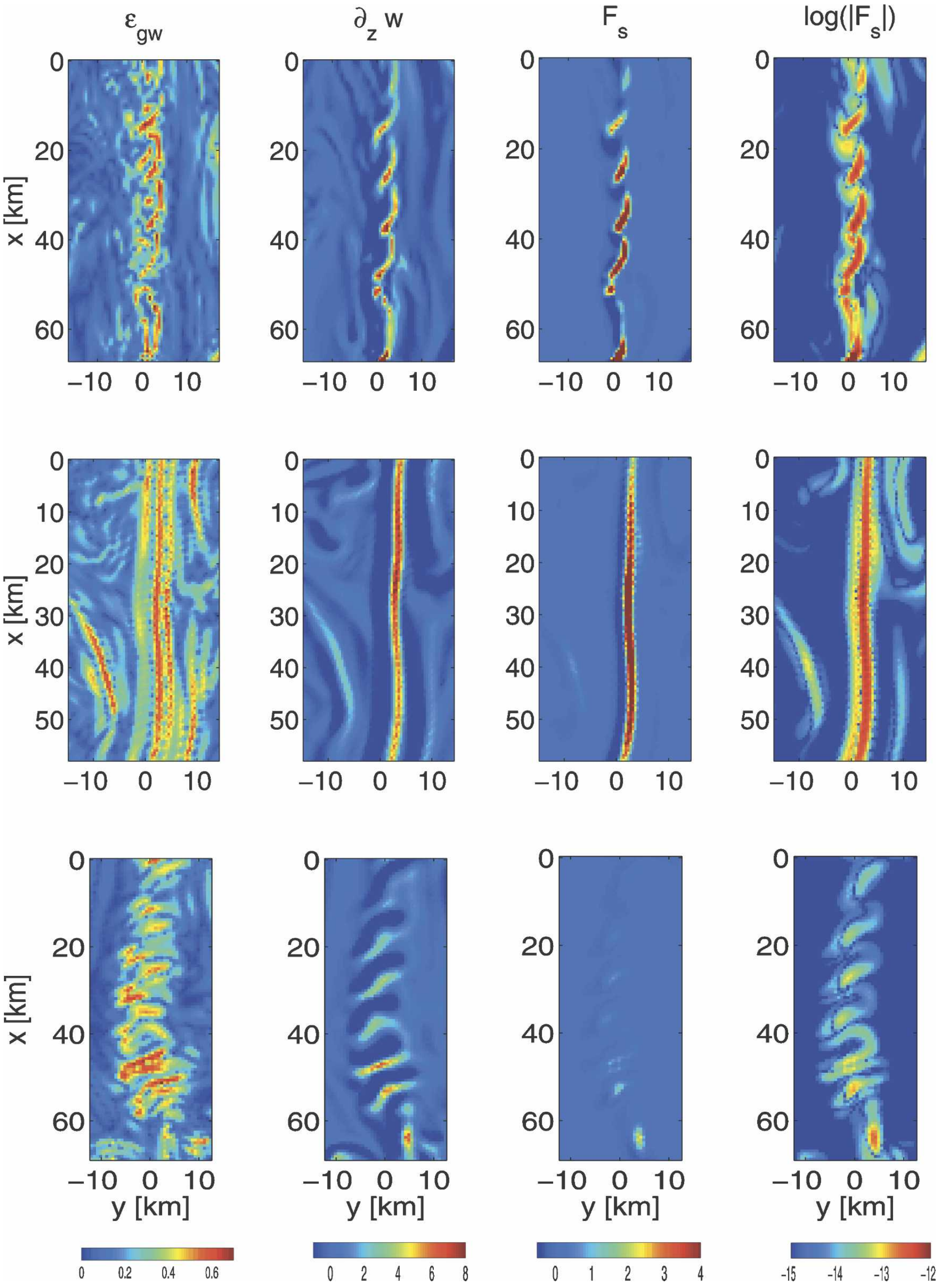

FIG. 20. Relative error in gradient-wind balance ϵ_{gw}, vertical divergence $\partial_z w$, and frontogenetic tendency due to straining F_s (with both linear and logarithmic contouring) for several submesoscale subregions: (top) the unstable frontal flow for case 3 of section 4; (middle) an evidently stable front whose location is indicated in Fig. 19; and (bottom) a flow region undergoing convective instability.

7. Summary

The phenomenon of submesoscale variability in an idealized eastern boundary current is analyzed in terms of its primary dynamical processes. Surface density fronts form in the regions of high strain on the flanks of mesoscale eddies. Frontogenesis sharpens them down to a horizontal scale of a few kilometers or less in association with an ageostrophic secondary circulation mostly confined to the surface boundary layer. This submesoscale process efficiently releases potential energy and acts effectively to restratify the upper ocean, even though only a small fraction of the domain is actively frontal at any given time. Many of the fronts exhibit submesoscale meanders indicative of a parallel-flow instability process, and many fronts evolve to become fragmented and develop into coherent vortices. The most consistent signature of instability is a positive conversion of potential energy associated with the frontal perturbations (i.e., $PK_e > 0$), usually associated with baroclinic instability. Submesoscale instability events are confined to near the surface and have a lateral scale not much larger than the mixed-layer deformation radius R_{ml} but much smaller than the mesoscale first baroclinic deformation radius R_1. This is consistent with baroclinic instability of the near-surface currents and stratification, either the classical balanced or anticyclonic ageostrophic types. Small regions with negative q_e and $\partial_z b$ develop near some surface fronts, especially when the alongfront flow is oriented downwind, but the resulting centrifugal and convective instabilities are not nearly as prevalent as the baroclinic instability. The flow remains close to satisfying a geostrophic or gradient-wind force balance most of the time. The main departures from balance are found in the vicinity of both stable and unstable fronts, and the unbalance patterns most strongly reflect the ageostrophic secondary circulation associated with frontogenesis.

In our simulations it seems to be typical for submesoscale fronts, frontogenesis, ageostrophic secondary circulation, frontal instability across a range of scales, and coherent vortices to occur simultaneously. There are still important open questions about frontal instabilities in the presence of active straining and their respective roles in the overall dynamical transition between oceanic mesoscale eddies and microscale turbulence.

Acknowledgments. The authors greatly appreciate discussions with Patrice Klein, Lien Hua, and Guillaume Lapeyre. This research was supported by ONR Grants N00014-04-1-0401 and N00014-05-10293 and NSF Grants OCE-0221177 and OCE-0550227. Many of the computations were made at the National Center for Supercomputing Applications.

REFERENCES

Barth, J., 1994: Short wavelength instabilities on coastal jets and fronts. *J. Geophys. Res.,* **99,** 16 095–16 115.

Bishop, C., 1993: On the behavior of baroclinic waves undergoing horizontal deformation. II: Error-bound amplification and Rossby wave diagnostics. *Quart. J. Roy. Meteor. Soc.,* **119,** 241–267.

Blumen, W., 1978: Uniform potential vorticity flow: Part I. Theory of wave interactions and two-dimensional turbulence. *J. Atmos. Sci.,* **35,** 774–783.

Boccaletti, G., R. Ferrari, and B. Fox-Kemper, 2007: Mixed layer instabilities and restratification. *J. Phys. Oceanogr.,* **37,** 2228–2250.

Capet, X., J. C. McWilliams, M. J. Molemaker, and A. F. Shchepetkin, 2008: Mesoscale to submesoscale transition in the California Current System. Part I: Flow structure, eddy flux, and observational tests. *J. Phys. Oceanogr.,* **38,** 29–43.

Castelao, R. M., T. P. Mavor, J. A. Barth, and L. C. Breaker, 2006: Sea surface temperature fronts in the California Current System from geostationary satellite observations. *J. Geophys. Res.,* **111,** C09026, doi:10.1029/2006JC003541.

Celani, A., M. Cencini, A. Mazzino, and M. Vergassola, 2004: Active and passive tracers face to face. *New J. Phys.,* **6,** 72, doi:10.1088/1367-2630/6/1/072. [Available online at http://www.iop.org/EJ/article/1367-2630/6/1/072/njp4_1_072.html.]

Dritschel, D., P. Haynes, M. Juckes, and T. Shepherd, 1991: The stability of a two-dimensional vorticity filament under uniform strain. *J. Fluid Mech.,* **230,** 647–665.

Eldevik, T., 2002: On frontal dynamics in two model oceans. *J. Phys. Oceanogr.,* **32,** 2915–2925.

Giordani, H., and G. Caniaux, 2001: Sensitivity of cyclogenesis to sea surface temperature in the northwestern Atlantic. *Mon. Wea. Rev.,* **129,** 1273–1295.

Haine, T., and J. Marshall, 1998: Gravitational, symmetric, and baroclinic instability of the ocean mixed layer. *J. Phys. Oceanogr.,* **28,** 634–658.

Hakim, G. J., C. Snyder, and D. J. Muraki, 2002: A new surface model for cyclone–anticyclone asymmetry. *J. Atmos. Sci.,* **59,** 2405–2420.

Harrison, D., and A. Robinson, 1978: Energy analysis of open regions of turbulent flows: Mean eddy energetics of a numerical ocean circulation experiment. *Dyn. Atmos. Oceans,* **2,** 185–211.

Held, I., R. Pierrehumbert, S. Garner, and K. Swanson, 1995: Surface quasi-geostrophic dynamics. *J. Fluid Mech.,* **282,** 1–20.

Hosegood, P., M. C. Gregg, and M. H. Alford, 2006: Submesoscale lateral density structure in the oceanic surface mixed layer. *Geophys. Res. Lett.,* **33,** L22604, doi:10.1029/2006GL026797.

Hoskins, B. J., 1974: The role of potential vorticity in symmetric stability and instability. *Quart. J. Roy. Meteor. Soc.,* **100,** 480–482.

——, 1982: The mathematical theory of frontogenesis. *Annu. Rev. Fluid Mech.,* **14,** 131–151.

——, and F. P. Bretherton, 1972: Atmospheric frontogenesis models: Mathematical formulation and solution. *J. Atmos. Sci.,* **29,** 11–37.

——, and N. V. West, 1979: Baroclinic waves and frontogenesis. Part II: Uniform potential vorticity jet flows—Cold and warm fronts. *J. Atmos. Sci.,* **36,** 1663–1680.

Juckes, M., 1995: Instability of surface and upper-tropospheric shear lines. *J. Atmos. Sci.,* **52,** 3247–3262.

Klein, P., B. Hua, G. Lapeyre, X. Capet, S. Le Gentil, and H. Sasaki, 2008: Upper-ocean turbulence from high-3D-resolution simulations. *J. Phys. Oceanogr.,* in press.

Lapeyre, G., and P. Klein, 2006: Dynamics of the upper oceanic layers in terms of surface quasigeostrophy theory. *J. Phys. Oceanogr.,* **36,** 165–176.

——, ——, and B. Hua, 2006: Oceanic restratification forced by surface frontogenesis. *J. Phys. Oceanogr.,* **36,** 1577–1590.

Mahadevan, A., and A. Tandon, 2006: An analysis of mechanisms for submesoscale vertical motion at ocean fronts. *Ocean Modell.,* **14,** 241–256.

McCreary, J., Y. Fukamachi, and P. Kundu, 1991: A numerical investigation of jets and eddies near an eastern ocean boundary. *J. Geophys. Res.,* **96,** 2515–2534.

McWilliams, J. C., 1985: A uniformly valid model spanning the regimes of geostrophic and isotropic, stratified turbulence: Balanced turbulence. *J. Atmos. Sci.,* **42,** 1773–1774.

——, and I. Yavneh, 1998: Fluctuation growth and instability associated with a singularity of the balance equations. *Phys. Fluids,* **10,** 2587–2596.

Molemaker, M. J., J. C. McWilliams, and I. Yavneh, 2001: Instability and equilibration of centrifugally-stable stratified Taylor-Couette flow. *Phys. Rev. Lett.,* **23,** 5270–5273.

——, ——, and ——, 2005: Baroclinic instability and loss of balance. *J. Phys. Oceanogr.,* **35,** 1505–1517.

Moore, D., and P. Saffman, 1975: The instability of a straight vortex filament in a strain field. *Philos. Trans. Roy. Soc. London A,* **346,** 413–425.

Müller, P., 1995: Ertel's potential vorticity theorem in physical oceanography. *Rev. Geophys.,* **28,** 277–308.

Narimousa, S., and T. Maxworthy, 1985: Two-layer model of shear-driven coastal upwelling in the presence of bottom topography. *J. Fluid Mech.,* **159,** 503–531.

Niiler, P., 1969: On the Ekman divergence in an oceanic jet. *J. Geophys. Res.,* **74,** 7048–7051.

Nurser, A. J. G., and J. W. Zhang, 2000: Eddy-induced mixed layer shallowing and mixed layer/thermocline exchange. *J. Geophys. Res.,* **105,** 21 851–21 868.

O'Sullivan, D., and T. J. Dunkerton, 1995: Generation of inertia–gravity waves in a simulated life cycle of baroclinic instability. *J. Atmos. Sci.,* **52,** 3695–3716.

Paduan, J., and P. Niiler, 1990: A Lagrangian description of motion in northern California coastal transition filaments. *J. Geophys. Res.,* **95,** 18 095–18 109.

Pedlosky, J., 1987: *Geophysical Fluid Dynamics*. 2d ed. Springer-Verlag, 710 pp.

Pierrehumbert, R., I. Held, and K. Swanson, 1994: Spectra of local and nonlocal two-dimensional turbulence. *Chaos Solitons Fractals,* **4,** 1111–1116.

Plougonven, R., and C. Snyder, 2007: Inertia–gravity waves spontaneously generated by jets and fronts. Part I: Different baroclinic life cycles. *J. Atmos. Sci.,* **64,** 2502–2520.

Samelson, R. M., 1993: Linear instability of a mixed-layer front. *J. Geophys. Res.,* **98,** 10 195–10 204.

——, and D. C. Chapman, 1995: Evolution of the instability of a mixed-layer front. *J. Geophys. Res.,* **100,** 6743–6759.

Shchepetkin, A. F., and J. C. McWilliams, 1998: Quasi-monotone advection schemes based on explicit locally adaptive dissipation. *Mon. Wea. Rev.,* **126,** 1541–1580.

Spall, M., 1995: Frontogenesis, subduction, and cross-front exchange at upper ocean fronts. *J. Geophys. Res.,* **100,** 2543–2557.

——, 1997: Baroclinic jets in confluent flows. *J. Phys. Oceanogr.,* **27,** 1054–1071.

Stone, P. H., 1966a: Frontogenesis by horizontal wind deformation fields. *J. Atmos. Sci.,* **23,** 455–465.

——, 1966b: On non-geostrophic baroclinic instability. *J. Atmos. Sci.,* **23,** 390–400.

Thomas, L. N., 2005: Destruction of potential vorticity by winds. *J. Phys. Oceanogr.,* **35,** 2457–2466.

——, 2008: Formation of intrathermocline eddies at ocean fronts by wind-driven destruction of potential vorticity. *Dyn. Atmos. Oceans,* in press.

——, and C. M. Lee, 2005: Intensification of ocean fronts by down-front winds. *J. Phys. Oceanogr.,* **35,** 1086–1102.

Wang, D., 1993: Model of frontogenesis: Subduction and upwelling. *J. Mar. Res.,* **51,** 497–513.

Zhang, F., 2004: Generation of mesoscale gravity waves in upper-tropospheric jet-front systems. *J. Atmos. Sci.,* **61,** 440–457.